• Original Paper •

Use of Targeted Orographic Smoothing in Very High Resolution Simulations of a Downslope Windstorm and Rotor in a Sub-tropical Highland Location※

Peter SHERIDAN[*1], Anlun XU[2], Jian LI[3], and Kalli FURTADO[1†]

[1]*Met Office*, *Exeter*, *EX*1 3*PB*, *UK*
[2]*Dali National Climate Observatory*, *Dali* 671003, *China*
[3]*State Key Laboratory of Severe Weather and Institute of Tibetan Plateau Meteorology*,
Chinese Academy of Meteorological Sciences, *Beijing* 100081, *China*

ABSTRACT

Nested simulations of a downslope windstorm over Cangshan mountain, Yunnan, China, have been used to demonstrate a method of topographic smoothing that preserves a relatively large amount of terrain detail compared to typical smoothing procedures required for models with terrain-following grids to run stably. The simulations were carried out using the Met Office Unified Model (MetUM) to investigate downslope winds. The smoothing method seamlessly blends two terrain datasets to which uniform smoothing has been applied — one with a minimum of smoothing, the other smoothed more heavily to remove gradients that would cause model instabilities. The latter dataset dominates the blend where the steepest slopes exist, but this is localised and recedes outside these areas. As a result, increased detail is starkly apparent in depictions of flow simulated using the blend, compared to one using the default approach. This includes qualitative flow details that were absent in the latter, such as narrow shooting flows emerging from roughly 1–2 km wide leeside channels. Flow separation is more common due to steeper lee slopes. The use of targeted smoothing also results in increased lee side temporal variability at a given point during the windstorm, including over flat areas. Low-/high-pass filtering of the wind perturbation field reveals that relative spatial variability above 30 km in scale (reflecting the background flow) is similar whether or not targeting is used. Beneath this scale, when smoothing is targeted, relative flow variability decreases at the larger scales, and increases at lower scales. This seems linked to fast smaller scale flows disturbing more coherent flows (notably an along-valley current over Erhai Lake). Spatial variability of winds in the model is unsurprisingly weaker at key times than is observed across a local network sampling mesoscale variation, but results are compromised due to relatively few observation locations sampling the windstorm. Only when targeted smoothing is applied does the model capture the downslope windstorm's extension over the city of Dali at the mountain's foot, and the peak mean absolute wind.

Key words: lee wave, turbulence, mountain, Tibetan Plateau, aviation, flow separation, Foehn, complex terrain

Article Highlights:

• 100 m horizontal grid spacing NWP simulations reproduce mountain wave and rotor flow.
• Spatially selective smoothing targeted only at very steep slopes results in enhancement of the fine scale flow detail.
• As a result, observed wind, and its spatial and temporal variability, are better reflected.

---

1. Introduction

Large-amplitude mountain waves resulting from stable flow over high mountains may be the source of downslope windstorms and lee rotors, resulting in very strong near-surface winds and elevated turbulence, and creating hazards for

surface and airborne transportation; the phenomena are well documented for many locations (for instance, Lilly and Zipser, 1972; Bougeault et al., 2001; Grubišić and Lewis, 2004; Jiang and Doyle, 2008; Grisogono and Belusic, 2009; Mayr and Armi, 2010; Kuzmi et al., 2015; Strauss et al., 2015; Elvidge et al., 2015; Elvidge and Renfrew, 2016; Moore, 2016; Beusch et al., 2018; Haid et al., 2022; Park et al., 2022), and have been extensively modelled (for instance, Durran, 1986; Doyle and Durran, 2002, 2007; Doyle and Smith, 2003; Gohm et al., 2004; Belušić et al., 2007; Reinecke and Durran, 2009; Sheridan and Vosper, 2012; Večenaj et al., 2012; Xue et al., 2020; Orr et al., 2021). Associated impacts may be difficult to predict, with different NWP models responding differently to the same inflow, and a strong dependence on model resolution, parametrizations, land-use data, and some situations being inherently very sensitive to small changes in inflow conditions (Reinecke and Durran, 2009).

When simulating small-scale phenomena, model performance is generally expected to improve when resolution is increased, for instance by maximising detail in the flow to better capture turbulent effects or highly local variations. A common frustration when doing this is the tendency of models with terrain-following grids to encounter difficulties with steep slopes. Terrain-following grids are widely used for operational forecasting and research (Steppeler et al., 2003), but introduce errors over steep terrain, due to the transformation of the curved coordinate surfaces onto a rectangular vertical grid for easier computational formulation (Gary, 1973), with the resulting introduction of metric terms into the equations of motion (Shaw and Weller, 2016; Shaw, 2018). This can lead to model instability, and a number of techniques to mitigate this with terrain-following models have been proposed (Klemp, 2011; Zängl, 2012; Weller and Shahrokhi, 2014). While errors may also be mitigated by shortening the model timestep, smoothing must be applied to allow simulations to proceed stably (Webster et al., 2003), and model failures due to steep terrain are a commonplace and often difficult problem in the development of new model configurations. Horizontal grid spacing places an upper limit on the steepest slope in a model terrain, and the existence of real terrain surfaces at all angles means that the steepest slope increases with decreasing model horizontal grid spacing. Since high resolution simulation seeks to benefit from the ability to model the response of the flow to fine terrain detail, a compromise must be struck between retaining detail, and ensuring the simulation runs stably, without too much computational cost. The balance of these concerns shifts for operational forecast models toward efficiency, compared to research models, but the same principle applies.

Commonly, a uniform smoothing procedure is applied to terrain data when creating a new model configuration. The steep slopes that would lead to model failures, however, may only exist in small areas of the model domain. This suggests that smoothing to mitigate their effects is excessive for other areas, if applied uniformly. In addition to affecting the dynamic response of the flow over the terrain, such "over-smoothing" of the majority of the terrain may significantly impact local and aggregate fluxes over a mountain area, and compromise comparisons with observations, where model and real terrain height and local morphology may be substantially different. For this study, a technique has been developed to locate slopes of problematic magnitude and to gradually and seamlessly incorporate locally increased smoothing only over areas containing them, while in the majority of the domain comparatively little smoothing is applied. This involves blending a minimally smoothed terrain dataset (which, without modificaton, would result in model crashes) with a dataset smoothed as usual (uniformly) as required for the model to run stably.

A nested simulation of a downslope windstorm/rotor case study using the Met Office Unified Model (MetUM) is used to demonstrate the impact of the targeted smoothing approach on the fine-scale structure of the flow. A nested simulation of the same case was performed by Xue et al. (2020) at the same resolution in the innermost domains, using the Weather Research and Forecasting (WRF) model, which reproduced observed features of the case. Large amplitude lee waves accompanied by a downslope windstorm and large, turbulent rotor in the lee of the ridge occurred in their simulation. The MetUM simulation was carried out as an opening step in a broader project to study mountain wave flows at the location.

In the remainder of the paper, the model setup, and observations used to examine its performance, are discussed in section 2; the targeted smoothing procedure is described in section 3; and a comparison of two simulations–one with targeted smoothing applied in all domains, and the other with it applied in the innermost domain only–against a control configuration using uniform smoothing, is carried out in section 4. The results of the study are summarised in section 5.

2. Numerical model set-up and observations

The simulations described in this study emerge from an attempt to repeat, using the MetUM, a case study simulation of a mountain wave accompanied by a downslope windstorm and rotor in the lee of Cangshan Mountain, Yunnan, China, that was carried out by Xue et al. (2020). Xue et al. (2020) used the Weather Research and Forecasting (WRF) model, with two-way nesting through domains of 9 km, 3 km, 1 km, 333 m and 111 m, driven by NCEP Final Analysis (NCEP-FNL) initial and boundary conditions. The location lies at the southeast edge of the Tibetan Plateau, and is home to the Dali National Climate Observatory, which hosts an array of observational instruments including a local network sampling mesoscale variation (hereafter termed a "mesonet") of sites measuring wind, temperature, humidity and other variables close to the surface. More details of the location and instrumentation are given by Xue et al. (2020). Locations of instruments measuring wind have been indicated in Fig. 1.

MetUM is a finite difference model on a latitude–longitude grid solving nonhydrostatic equations of motion using a semi-implicit, semi-Lagrangian dynamical core (Wood et

al., 2014). The MetUM configuration used employs a boundary layer scheme that blends the previous 1D boundary layer scheme (Lock et al., 2000) with a 3D Smagorinsky sub-grid scheme (Boutle et al., 2014), allowing seamless transition across resolutions from a more traditional NWP boundary layer scheme to one more commonly used in Large Eddy Simulations (LES). The radiation parametrization is based on Edwards and Slingo (1996), with topographic shading (affecting direct shortwave radiation) and skyview (affecting longwave radiation) implemented. The Smith (1990) sub-grid cloud scheme is used and the cloud microphysics scheme used is based on Wilson and Ballard (1999) with scale aware improvements (Boutle et al., 2014), again for seamless use across grid resolutions. The land surface is modelled using the Joint UK Land Environment simulator (JULES; Best et al., 2011), to which the MetUM is coupled. Gravity wave and convection parametrizations are not used in the nested domains (only in the driving global model).

The MetUM simulations for this study used one-way nesting driven by analysis and lateral boundary conditions derived from the Met Office Global Model, a global operational forecast configuration of MetUM. Nests centred at (25.79°N, 100.08°E) with grid spacing of 0.04°, 0.0135°, 0.0027° and 0.0009° were used, which at the equator would correspond to 4.4 km, 1.5 km, 300 m and 100 m spacing, and the latter numbers will be used to refer to the different domains throughout this manuscript. These are the default horizontal grid spacings set within the Met Office Regional Nesting Suite (RNS), which represents a framework designed to ease and standardise the production of simulations of this kind. Since the domains are relatively close to the equator, a rotated grid was not used. The domains are depicted in Fig. 1.

A vertical grid of 70 levels, stretched in the vertical, with the first temperature level at 5 m (velocity levels are vertical staggered, with the first at 2.5 m) and model top at 40 km is used in the nested domains (a similarly stretched grid with a model top at 80 km is used in the global driving model). The stretching is such that 16 levels exist below 2000 m AGL, with a spacing roughly 170 m at 1000 m.

The Global Land One-Kilometer Base Elevation (GLOBE) dataset on a 30 arc s grid is used to define the orography in the global model (Hastings and Dunbar, 1999),

while for the nested domains, data from the Space Shuttle Radar Topography Mission (SRTM) dataset (Farr et al., 2007) are used, on a 3 arc s grid (roughly 90 m). Details of required smoothing are discussed below.

The timesteps in each domain were reduced from their default values in the RNS of 180 s, 60 s, 12 s and 4 s, respectively for the 4.4 km, 1.5 km, 300 m and 100 m domains, to 60 s, 60 s, 2 s and 1 s, respectively. This was necessary to allow the model to run with the available smoothing options in some cases, and desirable to minimise required smoothing in others, in such complex terrain. Lateral boundaries were updated every 60, 30, 15 and 5 min, respectively, for the 4.4 km, 1.5 km, 300 m and 100 m domains. Model diagnostics were output generally as instantaneous values every 10 min, with 10 m wind components additionally output as 10 min averages at the same frequency.

MetUM version 11.7 has been used with the RA2T science configuration (geared towards tropical and sub-tropical locations; the Cangshan mountain area is categorised as a Subtropical Highland climate). The model simulations were initialised at 1200 UTC 22 January 2015. For a date this long past, the driving global model rerun from archived Met Office analyses must use the GA6.1 configuration (Walters et al., 2017). This represents version 6.1 of a standard configuration of MetUM for global running, optimised for NWP. The configuration must match the fields archived from the operational forecast at that time.

In models such as MetUM that use terrain-following grid surfaces, steep gradients that become more apparent in model terrain at high resolutions challenge the model's ability to run stably due to errors that can arise in the pressure gradient force calculation when grid surfaces tilt steeply (Shaw, 2018). The steeper gradients emerge with increasing resolution since, for pairs of points in real terrain a given distance apart, it is much easier to find pairs with steep mean gradient between them when that distance is small, than when it is large. Put another way, for a given height difference between two points, a steeper slope emerges if those points are closer together. To tackle this problem, the RNS employs smoothing of terrain data uniformly using a 1-2-1 filter. The 1-2-1 filter averages the target and adjacent points laterally at a grid box's sides to create a smoothed value. For a 1D filter, the target point has double the weight
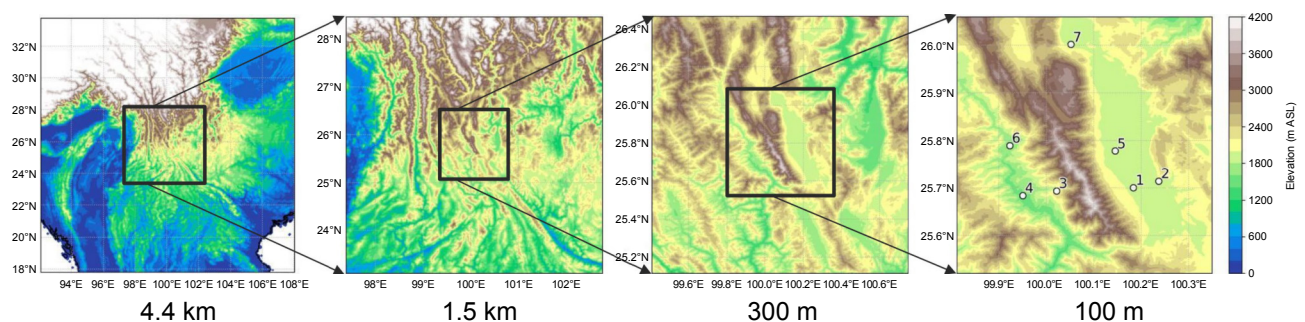

Fig. 1. Depiction of the areas of the one-way nesting domains used to run MetUM at 100 m horizontal grid spacing, showing terrain height and, rightmost, the 100 m grid spacing domain is used to indicate locations of surface measurement sites detecting wind.

of each adjacent point ("1-2-1"). A 2D filter repeats application in the two lateral directions, so that the target point has four times the weight in the average of each of the four laterally adjacent points. At user discretion, an option is available by default wherein further passes of the filter may be applied above 1500 m above sea level (ASL). This height is set by default, but includes almost all grid points in the innermost domains of the MetUM simulations over Cangshan mountain, so that the domains can be considered essentially uniformly smoothed (the height cut-off can also be straightforwardly modified). The number of passes required is influenced by the terrain encompassed (for instance the fraction of the Tibetan Plateau) and the timestep employed in a given domain. It was found that, for the simulation of the Cangshan windstorm case to run, 100, 10, 5 and 100 filter passes, respectively, were required for the 4.4 km, 1.5 km, 300 m and 100 m domains (options are 5, 10, 20, 35, 50, 75, 100). This resulted in the removal of undesirably large amounts of terrain information, particularly in the 4.4 km and 100 m domains. For this reason, a procedure was developed to target the extra smoothing in only those areas of each domain where steepness was sufficient to cause model stability problems. This method and how it has been applied to create several different experiments are described in the next section.

The Dali National Climate Observatory data used are available hourly as instantaneous or time averages of the detected wind vector, at 10 m height, except for one site (site 5) which is at 2.5 m height. Site 5 is on a platform on the lake close to the western shore. In order to be able to treat all the observations alike, a logarithmic wind correction using a roughness length of 0.0001 m (derived from modelling studies) was applied to adjust the site 5 measurements to be equivalent to those from the other sites.

3. Targeted orographic smoothing

3.1. *Targeted smoothing procedure*

The aim of this method is to create an orography ancillary that is smoothed only where necessary, without introducing discontinuities with the rest of the domain that is relatively unsmoothed. Therefore, a process of blending two uniformly smoothed orography ancillaries, one with minimal smoothing (a 1-2-1 filter applied once everywhere), and the other smoothed uniformly as much as necessary for the model to run stably (multiple passes of the same 1-2-1 filter), is used. To do this, a grid of weights, smoothly varying across the domain, is used to additively blend these two terrain datasets, and iteration performed until exceedances of a steepness threshold have been removed (or a maximum number of iterations carried out). This involves the following steps:

(i) The maximum slope in the more-smoothed dataset, S, is calculated.

(ii) Grid points in the less-smoothed ancillary that exceed this steepness threshold, S, are given a weight of 1.

(iii) A "dilation" filter is applied, which expands areas

of value 1 by five points in any direction.

(iv) This field is then converted from discrete binary values to an array of continuous floating point values, W, by applying a 2nd order Butterworth filter with a wavelength of six points.

(v) The terrain height at each point is calculated as the weighted mean of the more-smoothed height value and the less-smoothed height value, with weights of W and $(1 - W)$, respectively.

(vi) Items (i)−(v) are then repeated with this new dataset replacing the less-smoothed dataset. Iteration continues until either S is not exceeded or a maximum number of iterations is carried out.

This process is summarised in a flow chart in Fig. 2. The seamless, gradual spatial transition between areas of enhanced smoothing and areas with basic smoothing ensures that artefacts such as grid scale cliffs are not introduced. This process can be repeated for each nested domain. Figs. 3a–c show a comparison of the 100 m horizontal grid spacing domain with a single 1-2-1 filter application, 100 1-2-1 filter applications (found to be required for the model to run stably), and the blend of the two using the above targeting procedure, respectively. It is hard to distinguish Figs. 3a and 3c by eye, so difference plots for Fig. 3a vs. Figs. 3b and a vs. Fig. 3c, respectively, are shown in Figs. 3d and 3e. The difference in Fig. 3e is concentrated on a single chute off the ridge. The lack of substantial differences through the rest of the domain is emphasised by Fig. 3f, which uses a difference scale that is one order of magnitude finer. The mean terrain height in the 100 m domain was found to change by about 1 m after 100 passes of the 1-2-1 filter. The blend resulting from the targeted smoothing procedure differs from the 1-2-1 single pass data in mean height by about 2 cm. The orography in Fig. 3 can be compared to that in Fig. 1b or Fig. 3a of Xue et al. (2020).

To examine the impact of targeted smoothing on small scale flow features directly and via the driving conditions passed through from the coarser domains, several experiments were carried out using targeted smoothing selectively in the different domains. These comprise simulations named UNIFORM (no targeting in any domain, all uniform smoothed), TARG (targeted smoothing in all domains), TARG-INNER (targeted smoothing in the inner two domains) and TARG-INNERMOST (targeted smoothing in the innermost domain only). Principally the UNIFORM, TARG and TARG-INNERMOST simulations are used. UNIFORM is treated as a control simulation.

It was possible to compare the measured observation station heights with the height at the nearest point in the model in order to obtain a measure of the accuracy of the model terrain height at each observation point. For the UNIFORM simulation in the 100 m horizontal grid spacing domain, the most significant differences were at stations 2, 3 and 4, where differences of roughly 80 m, 40 m, and 150 m occurred, respectively. When targeted smoothing was used, sites 2, 3 and 6 had the largest differences, at roughly 60 m,
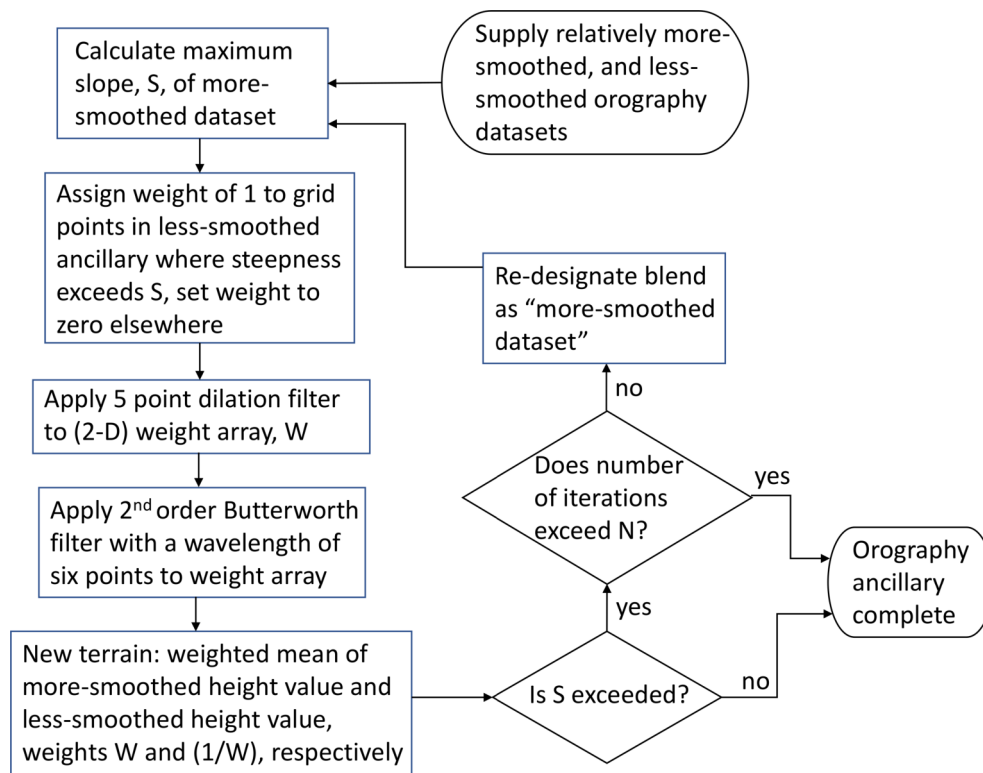
Calculate maximum slope, S, of more-smoothed dataset

Supply relatively more-smoothed, and less-smoothed orography datasets

Assign weight of 1 to grid points in less-smoothed ancillary where steepness exceeds S, set weight to zero elsewhere

Re-designate blend as "more-smoothed dataset"

Apply 5 point dilation filter to (2-D) weight array, W

Apply 2nd order Butterworth filter with a wavelength of six points to weight array

Does number of iterations exceed N? — no / yes

New terrain: weighted mean of more-smoothed height value and less-smoothed height value, weights W and (1/W), respectively

Is S exceeded? — yes / no

Orography ancillary complete

Fig. 2. Flowchart depicting the targeted smoothing process described in the text.

15 m and 20 m, respectively. For site 2 in both cases the small hill on which the site is located is underrepresented. At 1.5 km grid spacing, the average difference across all sites for UNIFORM is 108 m, for TARG, 62 m. At 4.4 km the average difference for UNIFORM is 380 m, for TARG, 200 m. The shape of the terrain around a site can also be significant for wind modelling, but has not been examined for this study.

4. Simulation results

4.1. *Examination of effects on instantaneous flow structure*

For looking at the broad, general flow structure, the UNIFORM simulation can be used. The vertical winds and 10 m horizontal winds from the 100 m domain for this simulation at 10:41 UTC, around the peak of the simulated event are shown in Figs. 4a and 4b. This time is close to the "peak" time of 10:10 UTC selected by Xue et al. (2020) for the event. A large mountain wave can be seen in the mid-troposphere vertical velocities [Fig. 4a]. These data are taken from level 35. Over a flat surface at sea level this would be at 4075 m height ASL, and will be between roughly 6000 m and 8000 m ASL in the area of Cangshan mountain due to the terrain following grid.

In the 10 m winds, a southeasterly along-valley flow exists at the termination of a downslope flow from Cangshan (which separates from the surface and rides over this along-valley flow). This flow separation can be seen in vertical

cross-sections through the wind at the same time in Figs. 5a and 5b. Within the along-valley flow [Fig. 4b] there are narrow "fronts" or "pulses" of intense wind that, by examining similar images for multiple times (not shown), were found to be quasi-periodic and propagate with the flow. The downslope flow, meanwhile, was found to be comparatively steady.

This structure, i.e. flow separation with an along-valley cross-flow underlying the separated jet from the downslope flow, contrasts with simple 2D conceptual pictures of rotors as an overturning and return flow beneath a wave crest, instead betraying a 3D structure to such flows. This is not unexpected, however, with precedents existing in the literature, resulting from the inevitable action of large scale pressure gradient forces and the confining geometry of a valley. For instance, rotor flows in the Owens Valley, Nevada, USA, with a not dissimilar scale and structure to the Erhai valley, exhibited a similar along-valley flow beneath separated downslope flow in windstorm cases (Sheridan and Vosper, 2012). Nevertheless, directly reversed flows can be seen highlighted by vectors plotted in Fig. 4, and a coherent area of substantial reversal of the in-plane flow component beneath the wave crest in Fig. 5, reflecting the 2D concept and associated turbulence.

Figures. 4c and 4d show how the features of the flow change when targeted smoothing is used in the innermost domain. A wealth of granular detail is added in Fig. 4d due to new small scale terrain detail causing local, terrain-locked perturbations directly. But also, there are qualitative differences between the two simulations at other scales. The
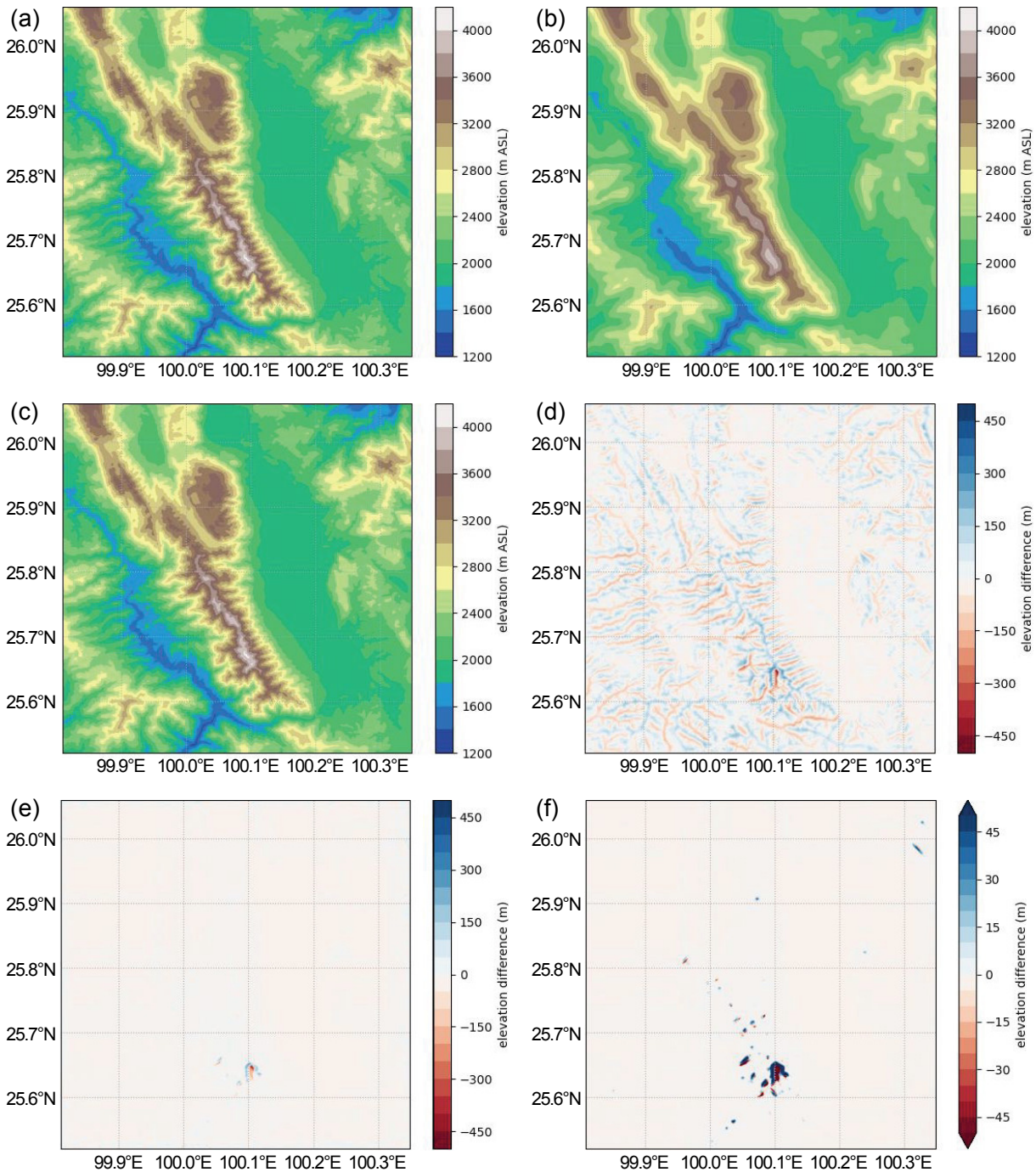
Fig. 3. (a) Orography in the 100 m horizontal grid spacing domain after a single pass of the 1-2-1 filter. (b) As in (a) but after 100 applications of the filter. (c) A blend of the datsets shown in (a) and (b) using the methodology in the text. (d) Plot of the difference between the terrain heights shown in (a) and in (b). (e) As in (d) but showing the difference between (c) and (a). (f) As in (e) but using a finer colour contour scale to highlight areas of smaller differences.

TARG-INNERMOST simulation contains multiple outflows that seem to be attached to corrugations on the lee side of Cangshan (these distinctive topographic elements feature prominently in various artistic depictions of the mountain around the region) and are more intense than the winds seen in the UNIFORM simulation. These features are persistent but not steady, pulsing in intensity, with pulses propagating

into the valley and sometimes crossing it entirely. Similar pulsing activity in jets of comparable width has been observed and simulated in the Bora flow that originates similarly as shooting flows (narrow supercritical flows, in the hydraulic analogy) from channels in the lee side of the Dinaric Alps (Belušić et al., 2007), with pulses of O(10 min) duration. Although data at intervals only of 10 min are avail-
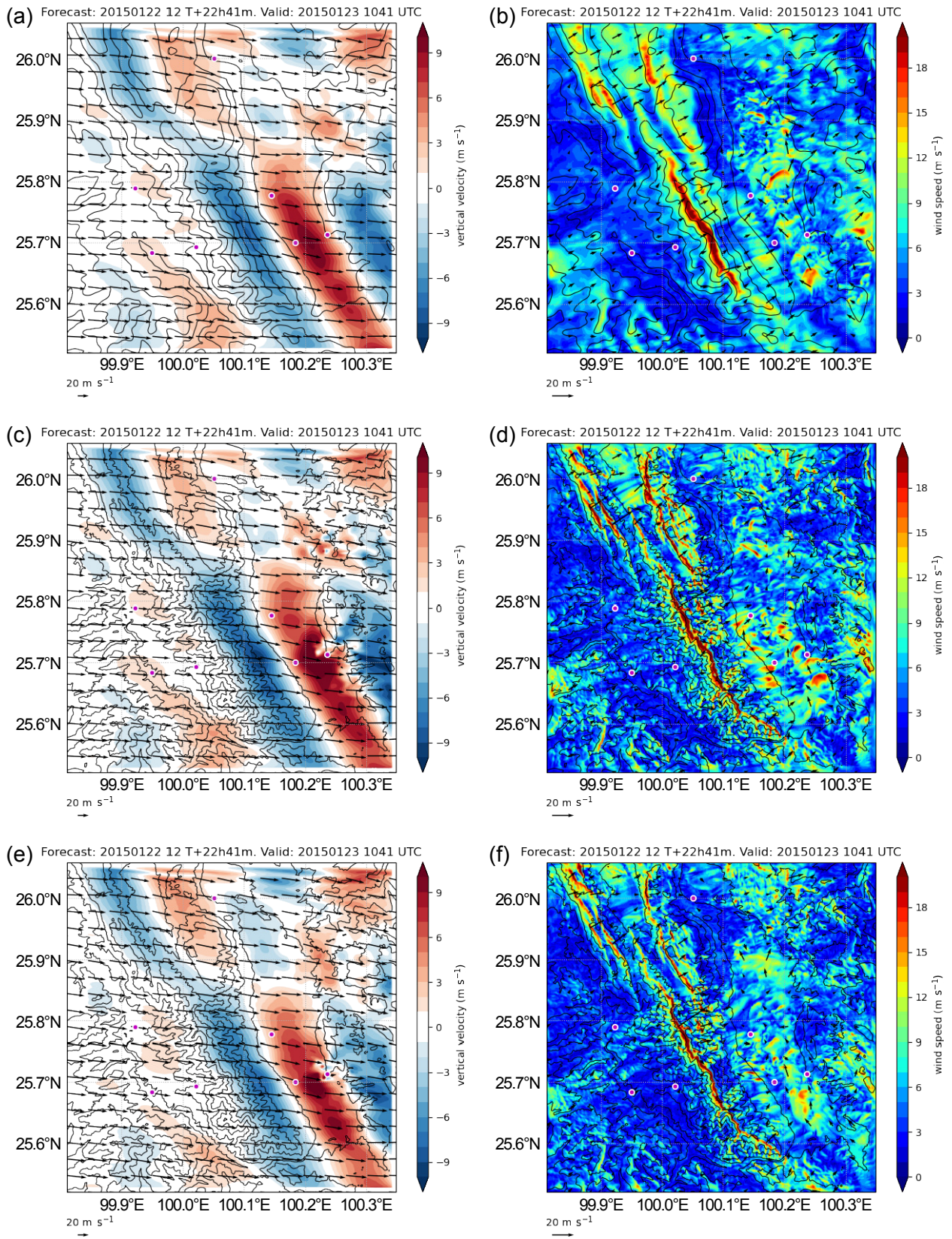
Fig. 4. Vertical velocity at model level 35 (lying between roughly 6000 m and 8000 m ASL depending on terrain height) from the 100 m horizontal grid spacing domain in (a) simulation UNIFORM, (c) from simulation TARG-INNERMOST, and (e) from simulation TARG, at 1041 UTC 23 January 2015. Panels (b), (d) and (f) are the same as (a), (c) and (e), respectively, but showing 10 m winds. Arrows represent horizontal wind vectors at the corresponding level, with magnitude indicated by the key at the base of each plot. Black contours represent the terrain height in 400 m intervals.

able from the MetUM simulations, studying the propagation of pulses across the valley (not shown) suggests a similar time period for these pulsations. Peltier and Scinocca (1990) also cite an O(10 min) period for pulsations in their simulated windstorm flows, and Doppler LiDAR studies of Boulder windstorms by Neiman et al. (1988). In all cases, Kelvin–Helmholz (KH) instablities (i.e. breaking shear waves) are cited as the origin, with Peltier and Scinocca (1990) suggesting that they represent a "choking" mechanism controlling the peak wind speed of the downslope flow.

A net effect of these outflows seems to be to push the flow-separation zone, on average, further east, while, at a given point along the ridge, it varies position from one time to the next. Instantaneously, the "line" of flow separation is resulting complex and hard to define, unlike for the UNIFORM simulation. Consequently, the along-valley flow in the TARG-INNERMOST simulation is much less coherent; notably, the along-valley pulses from the UNIFORM simulation are absent.

A further interesting (but understandable) difference between the UNIFORM and TARG-INNERMOST simula-

tions can be seen in vertical cross-sections through the flow. An east-west cross-section and a cross-ridge cross-section in Fig. 5 for each simulation, along the same planes used for cross-sections by Xue et al. (2020), show flow separation in both UNIFORM and TARG-INNERMOST simulations at the termination of the downslope wind on the valley floor. In addition, however, the steeper slope in the TARG-INNER-MOST simulation exceeds a threshold for leeside flow separation to occur, forming a stagnant bubble directly in the lee (this can be seen in extensive areas of weak flow in Fig. 4d on the lee slope before the flow reconnects near the base of the mountain).

A result of the finer edge formed by ridges in the TARG-INNERMOST simulation is a significant increase in the 10 m wind maxima in the domain, which occur over the most exposed and sharp ridges. Figure 6 demonstrates this for the time shown in Fig. 4. Wind speeds over the ridge do not exceed 25 m s^{-1} in the UNIFORM simulation, and exceedances of 20 m s^{-1} are confined largely to the highest ridge, whereas in the TARG-INNERMOST simulation, wind speeds exceed 20 m s^{-1} over numerous ridges, and
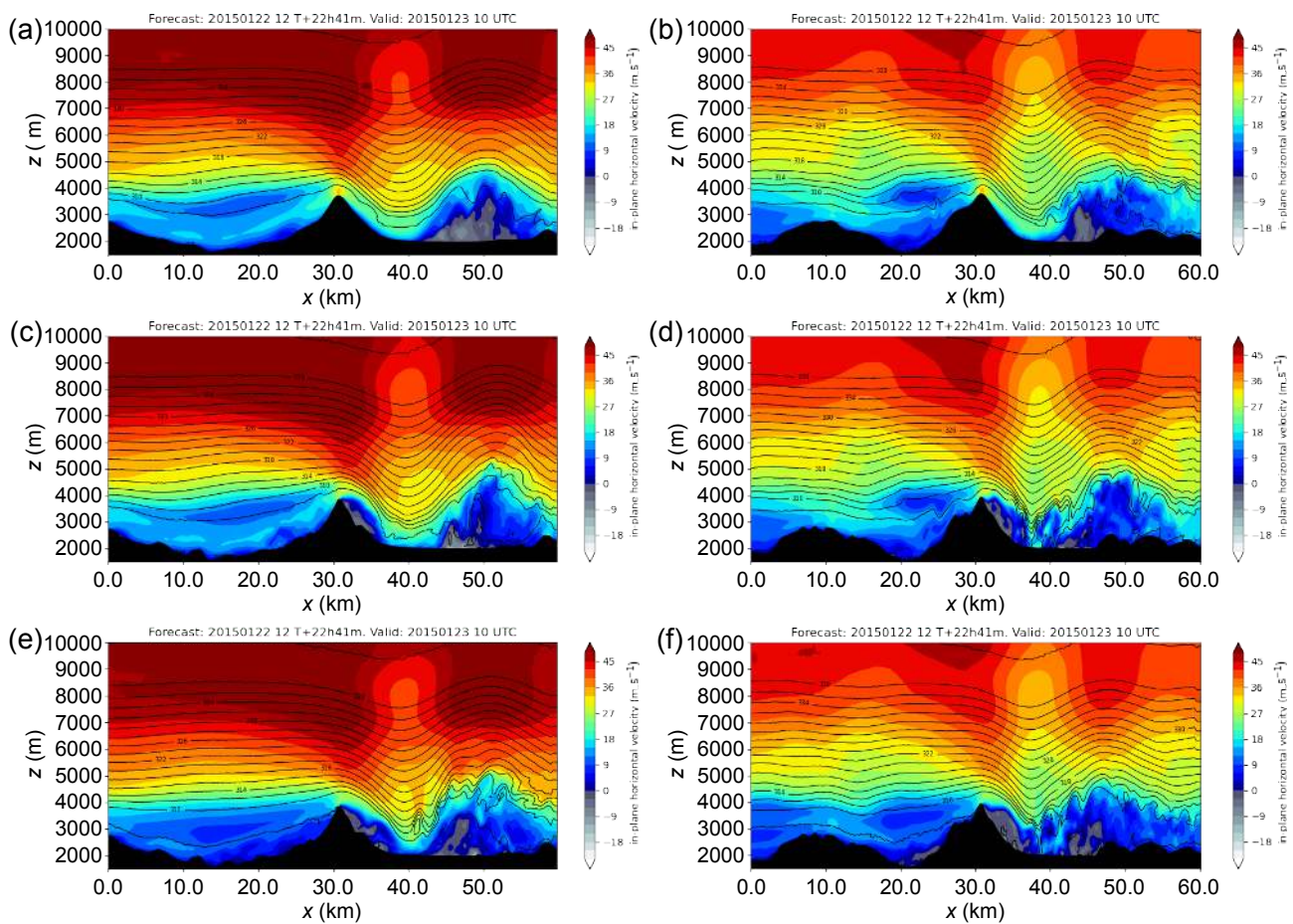

Fig. 5. Component of the wind resolved in-plane for a vertical cross-mountain cross-section corresponding to the west–east cross-section of Xue et al. (2020) shown at 1041 UTC 23 January 2015 for the 100 m horizontal grid spacing domain in (a) the simulation UNIFORM, (c) the simulation TARG-INNERMOST, and (e) the simulation TARG. Panels (b), (d) and (f) are the same as (a), (c) and (e), respectively, but showing the cross-section corresponding to the "northern" cross-section in Xue et al. (2020) (but extended here to cover an area similar to the west-east cross-section). The terrain cross-section is indicated in black at the base of the plot, and black contours indicate isentropes.
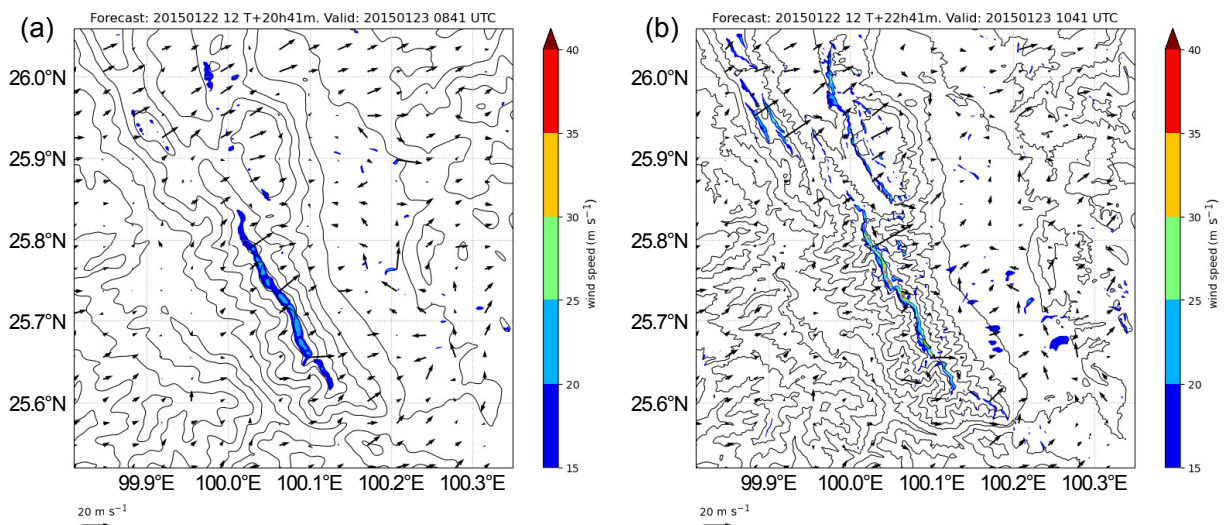
Fig. 6. Data from Figs. 4b and 4d, with the colour contour scheme revised to highlight high wind extremes.

35 m s^{-1} is exceeded in some areas of the main ridge.

4.2. *Time-averaged flow and quantification of temporal and spatial variability*

The differences between the two simulations can be examined in a more objective way by looking at fields averaged over time. Fig. 7 depicts the same fields as in Fig. 4, but averaged over a 2 hour period centred on 1100 UTC [this was a period used in a similar capacity by Xue et al. (2020)]. Comparing Figs. 7b and 7d, a less straight and well-defined average line of termination of the downslope flow (flow separation) in the TARG-INNERMOST simulations becomes obvious. The migration east of this zone compared to the UNIFORM simulation is also clear, and additionally is reflected in the phase of the waves aloft [Figs. 7a and 7c], as is the loss of coherency of the along-valley flow, especially downwind of the mountain in the central part of the domain where the valley widens. The persistence of the feature-locked outflows in TARG-INNERMOST is borne out. It seems that these combined with a significant increase in the speed of the downslope winds in the TARG-INNERMOST simulation are responsible for the increase in the penetration of the downslope flow, and change in the along-valley flow behaviour. This increase in speed may be related to increased nonlinearity of the flow resulting from greater steepness of the resolved terrain. The wave amplitude (quantified in terms of vertical velocity) is also larger, however, which may be another possible cause. This itself could be influenced by stronger nonlinear effects or enhanced by the increase in effective height of the terrain when it is better resolved.

In order to demonstrate objectively the increased time variation that results when targeted smoothing is used, wind standard deviation at each point for the same period was calculated and is depicted for the UNIFORM and TARG-INNERMOST simulations in Figs. 8a and 8b. A vector definition is used for this, where the standard deviation is taken as the root of the sum of squares of the standard deviation of each horizontal wind component. The location of the areas of

largest values are slighty different, but the standard deviation is generally significantly larger in the TARG-INNERMOST case throughout the domain. This includes over the valley floor, despite the presence of intense pulsations in the along-valley flow in the UNIFORM simulation, but most particularly at the foot of the mountains. The pulsating terrain-locked streaks also show as areas of large values in the standard deviation. Despite the downslope flow extending further east in the TARG-INNERMOST simulation, large values over the valley floor in the southern part of the domain commence further west, reflecting the more chaotic nature of the downslope flow termination. The largest values of wind standard deviation are found at the downwind edge of the immediate lee side flow separation bubble, at the reattachment point. Unsteadiness in this bubble, the chaotic location of reattachment along any given line, and the strong shear between the stagnant area and the separated downslope jet are consistent with this.

Visually, the 10 m wind fields in Fig. 4 appear to indicate greater spatial variability within the flow in the TARG-INNERMOST simulation. An attempt is made to quantify this, and eliminate the possibility, for instance, that the simulations differ only in the scale of variation, not its magnitude. For this, a speed-up parameter has been calculated across the innermost domain for each simulation at a given time. This represents a dimensionless streamwise perturbation of the flow, calculated as

$$\Delta s = \left(u_{10\mathrm{m}} - |\overline{\mathbf{u}_{10\mathrm{m}}}| \right) / |\overline{\mathbf{u}_{10\mathrm{m}}}|, \qquad (1)$$

where $u_{10\mathrm{m}}$ is the component, at a given point, of the wind in the direction of the mean 10 m wind vector $\overline{\mathbf{u}_{10\mathrm{m}}}$. The absolute value of this quantity is then mean averaged across the domain to give $\overline{|\Delta s|}$. An alternative calculation has also been considered using the mean absolute wind speed instead of the mean vector wind value, $\overline{|\Delta s_{mau}|}$, since influences on the flow direction other than waves (e.g. due to channelling along the Erhai valley) lead to different dominant
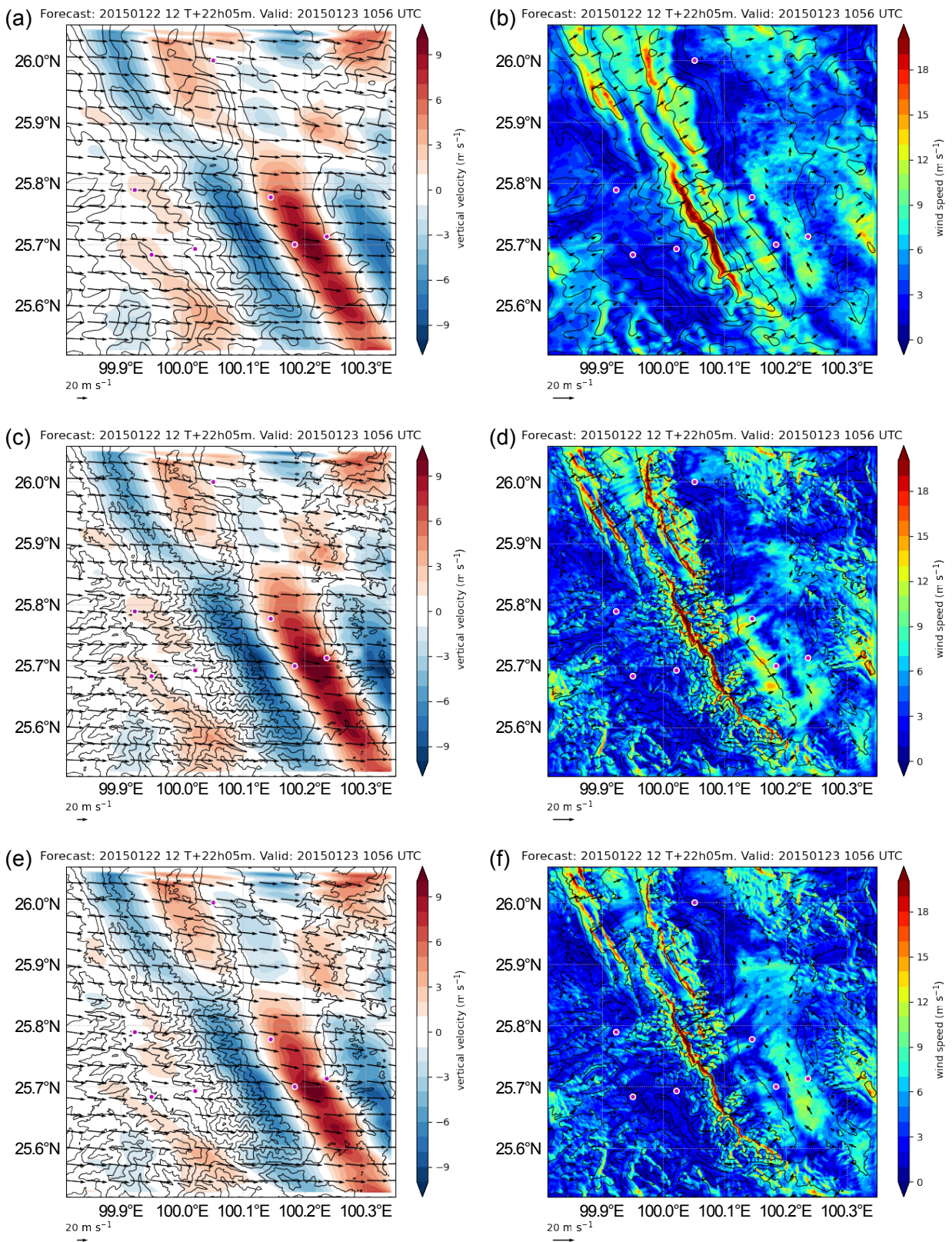
Fig. 7. Vertical velocity at model level 35 (lying between roughly 6000 m and 8000 m ASL depending on terrain height) from the 100 m horizontal grid spacing domain, averaged from instantaneous 10 min frequency fields between 1000 UTC and 1200 UTC 23 January 2015, in (a) the simulation UNIFORM, (c) from the simulation TARG-INNERMOST, and (e) from the simulation TARG. Panels (b), (d) and (f) are the same as (a), (c) and (e), respectively, but showing averaged 10 m winds. Arrows represent horizontal wind vectors at the corresponding level, with magnitude indicated by the key at the base of each plot. Black contours represent the terrain height in 400 m intervals.
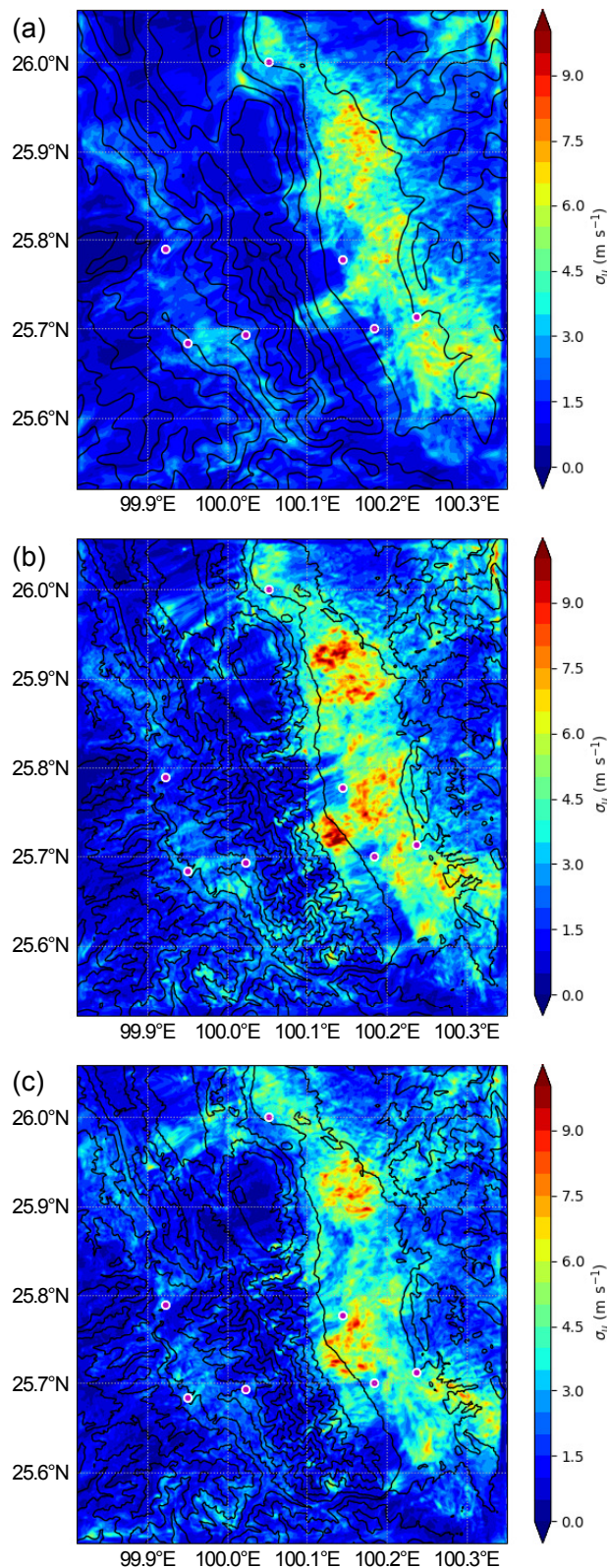
Fig. 8. Standard deviation of 10 m winds at each point in the 100 m horizontal grid spacing domain calculated from instantaneous 10 min frequency fields between 1000 UTC and 1200 UTC 23 January 2015 for (a) the simulation UNIFORM, (b) the simulation TARG-INNERMOST, and (c) the simulation TARG.

wind directions in different areas, causing the vector mean wind to be rather small, and the ratio in Equation 1 to tend to diverge to large values. The statistic based on the mean absolute value is more stable, although both statistics are useful.

Timeseries of both statistics for the 100 m domain of the UNIFORM and TARG-INNERMOST simulations are shown in Fig. 9. The same statistics calculated after using a perturbation field filtered for low pass using a Butterworth filter with a wavelength scale of 30 km is shown as a magenta line in each plot, and indicates the significance of large scale variation (such as due to mesoscale features or synoptic gradients) that exists in parallel with the wave-induced variation of interest and contributes to $\overline{|\Delta s|}$. $\overline{|\Delta s|}$ has been used in a previous publication (Sheridan et al., 2017) to quantify wave effects on low-level winds over the UK for forecasting purposes (and is currently used in some Met Office forecast products). In that application, a wind speed threshold was imposed to indicate where the statistic can be trusted to reflect variability and not merely low wind. The same methodology is applied here, and a 5 m s^{-1} threshold used. A bold black horizontal line is drawn in each plot to indicate the period in which this condition is statisfied. The wind averages used in the speed-up calculation themselves are shown in Fig. 9c.

Figure 9a depicts $\overline{|\Delta s|}$ for TARG-INNERMOST and UNIFORM. $\overline{|\Delta s|}$ is somewhat larger for TARG-INNERMOST than for UNIFORM. The mean vector wind is weaker in TARG-INNERMOST and partly responsible for this. The mean absolute speed is also generally lower for TARG-INNERMOST, but during the period of highest winds, which includes the period of most interest for the case, the differences in mean absolute speed are minimal [Fig. 9c]. The mean wind magnitude being similar, while the magnitude of the mean wind vector is different, indicates greater directional variability in the simulation where the magnitude of the mean wind vector is smaller (TARG-INNERMOST). This means that differences in $\overline{|\Delta s|}$ between the two simulations do indeed represent greater spatial variability occurring in TARG-INNERMOST. In the period of the peak of the windstorm, larger values also occur in $\overline{|\Delta s_{mau}|}$ for TARG-INNERMOST, confirming this. Note, the dashed line in Figs. 9a and 9b represents a terrain-dependent threshold of $\overline{|\Delta s|}$ extrapolated from values used by Sheridan et al. (2017) to indicate possible rotor formation. The threshold for UNIFORM has been used. Due to the extrapolation, the threshold line should not be interpreted too rigorously as a "rotor line". Nevertheless, the TARG-INNERMOST simulation does clear this indicative level more convincingly than the UNIFORM simulation. By all these objective measures then, an increase in flow variability in TARG-INNERMOST is borne out as a quantifiable outcome of increased granular detail in the simulated terrain.

The question remains, however, whether the increase in flow variability represents a trivial injection of flow detail at the small scales, or a deeper change in characteristics of the
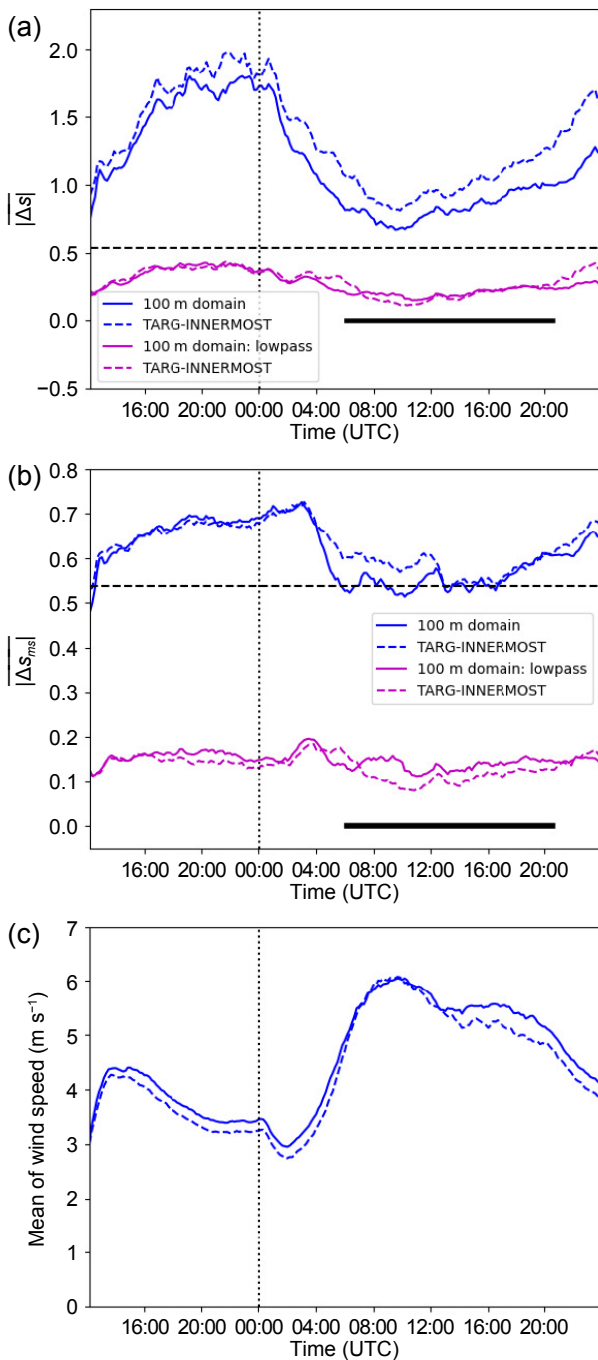
Fig. 9. Domain mean absolute speed-up values over time and mean absolute wind speed for the UNIFORM simulation (solid lines) and the TARG-INNERMOST simulation (dashed lines) in the 100 m horizontal grid spacing domain during each simulation. Quantities are (a) $\overline{|\Delta s|}$, (b) $\overline{|\Delta s_{maul}|}$ (see text), (c) mean absolute wind speed over the 100 m domain. In (a) and (b), the blue lines represent the values with no filtering applied to the wind perturbations, while the magenta lines represent the same statistics calculated after filtering the perturbation field filtered for low pass using a Butterworth filter with a wavelength scale of 30 km. A vertical dotted line indicates 0000 UTC. A horizontal dot-dashed line indicates a nominal "rotor" threshold defined by resolved orographic variability (see text). The thick horizontal black line indicates a period with mean wind above 5 m s⁻¹.

flow, potentially traversing scales. Changes such as outflow jets due to the introduction of terrain channels in the lee slope, represent new flow features that propagate well beyond the terrain features causing them, and so are not purely local, indicating a deeper change, from a qualitative point of view. To further, quantitatively, assess at what scales the extra flow variability in the TARG-INNERMOST simulation is being introduced, $\overline{|\Delta s|}$ and $\overline{|\Delta s_{maul}|}$ have been recalculated after applying high/low pass Butterworth filters to the along-flow perturbation fields using a range of filter scales. Scales of 8 km, 3 km and 1 km were used. The same method was used as that to create the low pass filtered perturbations corresponding to the magenta lines in Fig. 9 (where instead a scale of 30 km was used). In high pass, these filter scales remove or attenuate progressively more of the small scale flow variation, until only the smallest resolved scales remain.

The 1-2-1×100 filtered 100 m horizontal grid spacing orography used in UNIFORM was examined by eye compared to the unfiltered 300 m and 1.5 km domains' orography. In the 1-2-1×100 filtered 100 m grid spacing terrain, the smallest well-defined features were observed to be larger in scale than those in the unfiltered 300 m terrain, and smaller in scale than in the 1.5 km terrain, perhaps comparable to what would be well-resolved in unfiltered terrain on a grid of around 800 m spacing (an eightfold increase in the minimum scale of terrain features due to smoothing in UNI-FORM, compared to the majority of the equivalent TARG-INNERMOST domain). This scale defines a lower limit on the size of terrain features that will be effectively resolved within the model terrain, and thus in turn, a similar lower limit on the scale of immediate direct effects the terrain may have on the flow in the UNIFORM simulation: if a terrain feature can be considered well-resolved when it is represented across 8 grid points (Skamarock, 2004), then only direct terrain effects at scales of 6.4 km and above become well represented, and are under-represented below that scale. Thus we can expect the results of filtering at the chosen filter scales to have considerable sensitivity to the differences between the UNIFORM and TARG-INNERMOST simulations.

The results for $\overline{|\Delta s_{maul}|}$ for the two simulations with each of the three new filter scales are shown in Fig. 10. Predictably, as the filter scale decreases, for both simulations, the variability represented in the high pass data decreases, and that in the low pass data increases, as the low partition contains more and more of the range of resolved scales. In all cases, the low pass $\overline{|\Delta s_{maul}|}$ is larger for the UNIFORM case, and the high pass smaller. This is unlike the result when a 30 km filter scale was used (Fig. 9), and seems to suggest that the introduction of finer terrain detail causes a shift of variability from larger (but below 30 km) scales to smaller scales.

Focusing on the period of stronger winds (indicated in extent by the bold black line in Fig. 10), the high pass results for the two simulations continue to be offset similarly for all filter scales. By itself, this might suggest that the

scale transfer of variability in the TARG-INNERMOST simulation deposits into the smallest scales, below 1 km, elevating
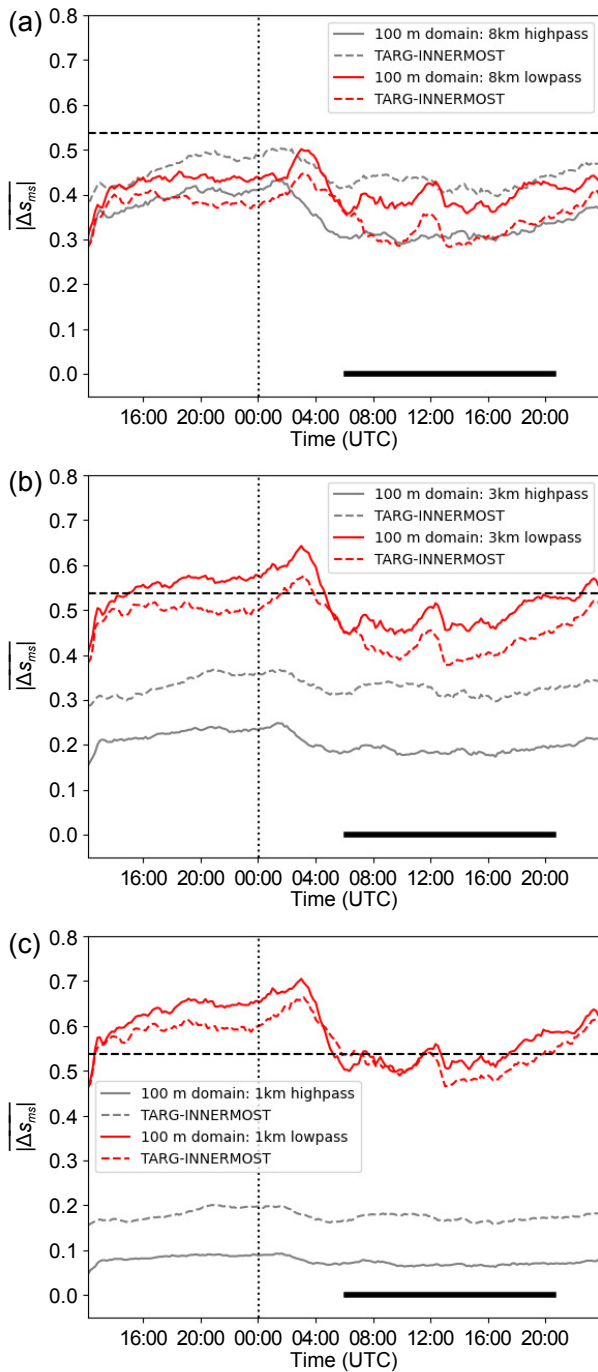

Fig. 10. Domain mean absolute speed-up values over time, calculated using fields to which a Butterworth filter of a given cutoff scale has been applied to create low pass (giving the red lines) and high pass (grey lines) datasets in the 100 m horizontal grid spacing domain, for the UNIFORM simulation (solid) and the TARG-INNERMOST simulation (dashed), over the duration of each simulation. The filter scale in each case is: (a) 8 km, (b) 3 km, (c) 1 km. A vertical dotted line indicates 0000 UTC. A horizontal dot-dashed line indicates a nominal "rotor" threshold defined by resolved orographic variability (see text). The thick horizontal black line indicates a period with mean wind above 5 m s^{-1}.

the high pass trace regardless of the filter scale. The low pass filtered results for the two simulations, however, converge as the filter scale decreases. This suggests that the net down-scale transfer of variability results in a decrease in between 8 km and 30 km scales, but a net increase in variability between 3 km and 8 km scales, and a greater increase between scales of 3 km and 1 km, as well as the (greater still) increase at sub-km scales.

The scale range where variability is lost in the TARG-INNERMOST simulation, between 8 km and 30 km, interestingly contains the horizontal wavelength of the waves aloft, and the principal scale of the mountains/valley. The overall implication seems to be that larger scale coherent features within the domain (shaped by the waves or the mountain/valley scale) are disturbed by features that occur on smaller scales, not simply that more detail is introduced at the smallest scales as a simple imprint of the terrain. An example of this is the transformation of the along-valley flow that is coherent and strong in the UNIFORM simulation but becomes far less so in TARG-INNERMOST as the jets emanating from the small channels in the Cangshan lee side cut across the valley. These new flow features emerge from flow over terrain features that were previously poorly represented due to smoothing.

4.3. Effect of targeted smoothing in the outer domains

The previous subsection isolated the impact of targeted smoothing in the innermost domain – i.e. with the same conditions driving the domain with the finest resolution and the most detail, in the orography and in flow dynamics. An experiment was also performed where targeted smoothing was applied in all domains, so that finer orographic detail became available in all resolutions throughout the nested set-up (termed "TARG"). This resulted in instantaneous fields in the 100 m domain that were ostensibly similar to those in the TARG-INNERMOST domain, as can be seen in Figs. 4 and 5, although seemingly with the downslope flow, and 10 m winds in general, a little weaker. In animated sequences of the 10 m winds, the same penetration of pulses across the valley from the channels on the lee side of Cangshan that were present in the TARG-INNERMOST simulation can also be seen in the TARG simulation (not shown).

The time averaged fields in Fig. 7f thus exhibit some of the same filamented structure as in Fig. 7d for TARG-INNERMOST, but thanks to the relative weakening of the downslope flow, the vector mean winds at the base of the ridge are weaker. Their appearance as being weaker than those for the UNIFORM simulation will be partly due to increased variability in this area in the TARG simulation compared to UNIFORM. A further effect seems to be the relative preservation intact of an along-valley flow similar to that for UNIFORM, with disturbance due to downslope outflows being less intense than for TARG-INNERMOST. The averaged vertical velocities are also weaker for TARG (Fig. 7e). It is telling that despite this diminution of wind strength in the TARG simulation compared to UNIFORM or TARG-INNERMOST, the temporal standard deviation still remains stronger in the

TARG simulation than that in the UNIFORM simulation (Fig. 8c).

Mean winds across the 100 m domain are weaker (whether measured by the $|\overline{\mathbf{u}_{10m}}|$ or the mean absolute speed) for TARG than for the UNIFORM or TARG-INNERMOST simulations, and it seems that the increased orographic detail in the outer domains is introducing a stronger sink on momentum – in effect there is an increase in resolved drag and blocking. This could be regarded as UNIFORM or TARG-INNERMOST having insufficient drag/blocking in the outer domains, since resolved effects are "missing" and sub-grid parametrizations do not take into account any smoothing the orography has undergone. A method to incorporate resolved orographic variation lost to smoothing into the sub-grid fields is being developed currently, and this would be expected to give better convergence between the TARG and TARG-INNERMOST simulations in this respect. A further experiment with targeted smoothing applied in the two inner domains (TARG-INNER) was found to give results closely resembling those of TARG-INNERMOST (not shown), indicating that the larger 1.5 km and 4.4 km horizontal grid spacing domains are more crucial than the smaller 300 m domain in determining the overall strength of winds experienced in the innermost domain.

4.4. *Comparison with observations*

Having discussed the impact of smoothing techniques, it is important to consider how this affects the accuracy of the model in reproducing aspects of the observed flow. As a basic exercise, the magnitude of the mean wind vector ($|\overline{\mathbf{u}_{10m}}|$) and the mean absolute wind speed measured across the 6 out of 7 sites in the Dali mesonet measuring wind (only 6 out of the 7 were in operation during the rotor event) are compared with the equivalent data obtained from the nearest model grid points in each nested MetUM domain, as a function of time in Fig. 11. Data are shown for the UNIFORM and TARG-INNERMOST simulations. Although instantaneous observations are available for comparison with the instantaneous (at 10 min intervals) data from the model, 10 min averages of the observations and model data are used for all comparisons (the observations are available at 1 hour intervals). Shorter averaging periods were found to produce significantly noisier plots that were more difficult to interpret.

The observed mean absolute winds peak at 0900 UTC 23 January 2015, and are somewhat variable from hour to hour after this. Interestingly, the mean *vector* drops significantly through the nominal "peak" period of the event, before rapidly recovering at 1300 UTC, while the mean absolute wind maintains relatively high values. This indicates that the mean vector is affected by wind directions being highly diverse between different surface measurement sites, while the wind at each individual site remains strong (though still somewhat variable). Of the simulations, in the innermost domain, the TARG-INNERMOST simulation reproduces mean absolute winds best, reproducing the

observed peak at about the same time, although it subsequently drops compared to the observed values. The mean vector winds are qualitatively similar in the two simulations, both capturing the drop to low values around the time of that observed between 1000–1300 UTC, but the timing of the two peaks is better in the UNIFORM simulation.

Comparisons of wind speed and direction for sites 1 and 2 in the lee of the mountain are shown in Figs. 12 and 13. Site 1 is in a farmland area on the western shore of Erhai Lake, but which we will term Dali, due to its proximity to Dali city. Site 2 is on a hill at the eastern shore of Erhai Lake at around the same latitude.

Site 1 experienced erratic wind direction switching between up-valley and roughly west-northwesterly, and increasing wind speed up to 0800 UTC, with winds reaching high values around 9 m s^{-1} from 0900 UTC and peaking at 1200 UTC over 9 m s^{-1}, while staying more consistently roughly west-northwesterly after 0800 UTC until 1200 UTC, after which a transition to consistently up-valley occurs. This signifies the gradual onset and subsequent recedence of a downslope windstorm over Dali. Evidence for this windstorm is essentially absent in the UNIFORM case, where westerly winds do not reach this far east. In the TARG-INNERMOST simulation, meanwhile, the windstorm is represented, with a peak in observed winds at 1000 UTC at over 9 m s^{-1} reached, although the associated winds are more west-southwesterly in direction.

Site 2 experienced instead a persistent and very strong up-valley flow for the whole period between 0600 and 1800 UTC. Neither model reproduces fully the strength of this flow, though UNIFORM fares slightly better, and the more consistent up-valley flow in the UNIFORM simulation better captures the persistent up-valley wind direction. In the TARG-INNERMOST simulation, more turbulent effects on wind direction occur, related to the interference of the outflows from the leeside channels that become resolved in that simulation, of the kind that affect Dali further west more directly, but in the 10 min averages these are not very apparent due to the averaging interval roughly matching the periodicity of outflows. Winds at site 2 in the WRF simulation by Xue et al. (2020) were similarly, if not more disturbed. Although the wind strength at site 2 is not reproduced in MetUM, it is clear from Fig. 4 that in all the simulations, up-valley winds over Erhai Lake of comparable or greater strength are commonplace, including at locations very close to site 2. Also, it is significant that, while site 2 is around 110 m above the lake surface on a small hill, the height differential in the model is only 30–50 m (see end of section 3.), indicating a much smaller hill which would be expected to result in weaker wind exposure.

The up-valley flow is consistent with the synoptic scale pressure gradient. The strength of the wind in this up-valley flow may, in addition to any height effects, be affected by the perturbation pressure field from the waves, however. Beneath a wave crest, just downwind of its peak, a positive pressure perturbation should exist. The simulated wave amplitude in Fig. 4 seems strongest along the valley at around
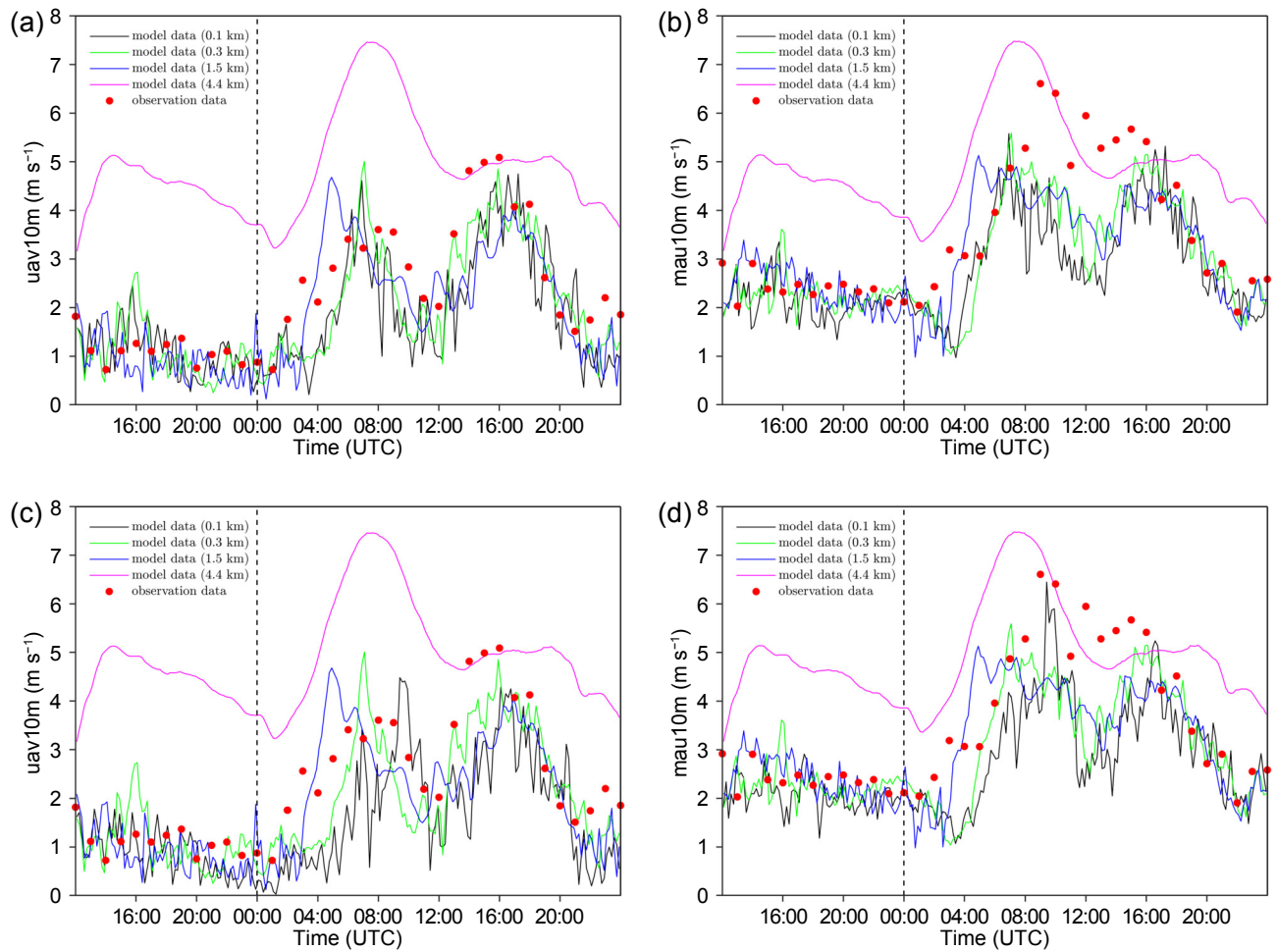
Fig. 11. Timeseries of (a), (c) mean 10 m wind vector magnitude and (b), (d) mean 10 m absolute wind speed across 6 sites measuring wind from the Dali National Climate Observatory mesonet, using 10 min average wind data, and the nearest point to each site from the nested MetUM domains (using instantaneous data), plotted over time during the 23 January 2015 windstorm case. Simulation data are from the (a), (b) UNIFORM and (c), (d) TARG-INNERMOST simulations. A vertical dashed line indicates 0000 UTC.

25.7°N, and this may cause a diminution of the up-valley pressure gradient south of this latitude, and an enhancement north of it. This would be consistent with the underestimation by the simulations of the wind at site 2. If the distribution of wave amplitude along-valley, or the overall amplitude of the waves, was different from that simulated, it may help explain the discrepancy. It may be possible in future work to analyse this if pressure measurements taken at the observation sites have sufficient sensitivity. Figure 7 shows that the time average winds in the area of site 2 are weak relative to other areas close by, especially to the south, supporting this. The periodicity of transient features that contain high winds in this and other areas of the innermost domain is, as stated, around 10 min, so that increasing the frequency of model output, at the observation site locations at least, would have a clear benefit as regards proper sampling of the wind variability, including high wind extremes at these locations.

Wind comparisons were performed at the other individual sites, but are less informative from the point of view of assessing the performance in the windstorm and figures have not been included. In general, there are similarities and differences between the model and observations at these sites for both simulations, with neither performing very badly, and overall, the two simulations perform comparably.

Speed-up values may again be evaluated, across the 6 operational wind measuring sites, to investigate spatial variability. $\overline{|\Delta s|}$ across the array of observation site locations was found to scatter to large values due to the small values of $|\overline{\mathbf{u}_{10m}}|$ that occur in both the observations and the model, and the relatively few points involved, making it a less useful statistic, and therefore the focus is instead on $\overline{|\Delta s_{mau}|}$.

Figures 14a and 14b compare values of $\overline{|\Delta s_{mau}|}$ from the model with those observed, for the UNIFORM and TARG-INNERMOST simulations respectively. Generally, the $\overline{|\Delta s_{mau}|}$ values from the observations are larger than those from the model, which is unsurprising since there will always be variability in the observations that is not resolved in the model (this has been found previously to be the case with data from the 1.5 km model examined by Sheridan et
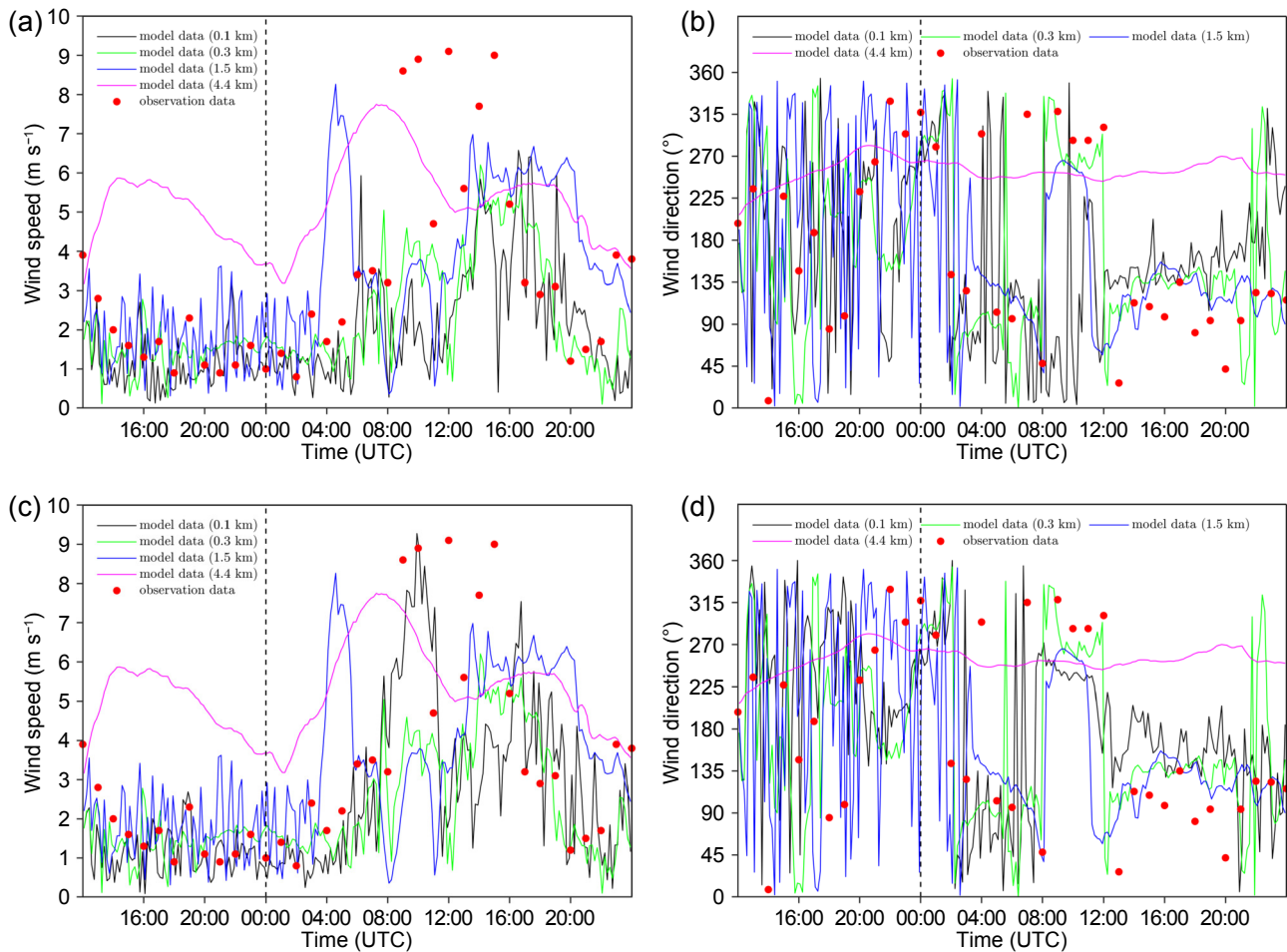
Fig. 12. (a), (c) Observed wind speed *vs.* time and (b), (d) observed wind direction *vs.* time for site 1 during the event. Overlaid are the instantaneous wind speeds at the nearest point from each of the nested domains (see colour key) for (a), (b) the UNIFORM simulation, (c), (d) the TARG-INNERMOST simulation. A vertical dashed line indicates 0000 UTC.

al., 2017).

We may recall that a threshold was used earlier to suggest that $\overline{|\Delta s_{mau}|}$ values should only be treated as meaningful for a period around the peak of the event, when winds are relatively strong. If we confine attention to the period between 0600 and 1800 UTC 23 January 2015, where this applies, it can be seen that, generally, comparable values to those observed are seen in the innermost domain, with spatial variation generally much more bland in the outer domains.

Restricting further between 0800 and 1200 UTC, when the nominal "peak" of the event occurs, the largest observed value occurs at 1100 UTC, remaining high for some hours. This is not matched in the model, although TARG-INNER-MOST comes closer, with a significant peak just after 1000 UTC, and generally reaching high values, though also being more variable.

After 1200 UTC, when the downslope windstorm recedes and the along-valley flow reasserts dominance, the 1.5 km model result compares similarly to the two innermost domains. When targeted smoothing is applied in the 1.5 km domain (not shown), the agreement with observations for that domain surpasses the inner domains for that period,

until 1600 UTC. This probably reflects the relatively simple structure of the up-valley flow, with the contrast between the along-valley cross-flow and the rest of the domain deciding the value of $\overline{|\Delta s_{mau}|}$. The 4.4 km domain performs uniformly badly, being too coarse to even adequately resolve the valley and its axial flow, regardless of whether or not targeted smoothing is applied.

Another way of examining the spatial flow variability in the model relative to that observed across the 6 sites is via the ratio of $|\overline{\mathbf{u}_{10m}}|$ to the mean absolute wind speed, which is plotted for the observations and the four simulation domains in Fig. 14c and 14d. This is similar to the wind "persistence", but involving an equivalent calculation in time, rather than space, to quantify the consistency of the wind direction over time (Farrugia and Micallef, 2006; Jemmett-Smith, 2014). A value of 1 indicates a perfectly consistent wind direction across all sites, with values below 1 indicating greater directional variability across sites. As a result, the rather uniform wind across the area in the 4.4 km domain gives values close to 1.

During low wind periods in the earliest and latest parts of the timeseries, both the observed and modelled parameter
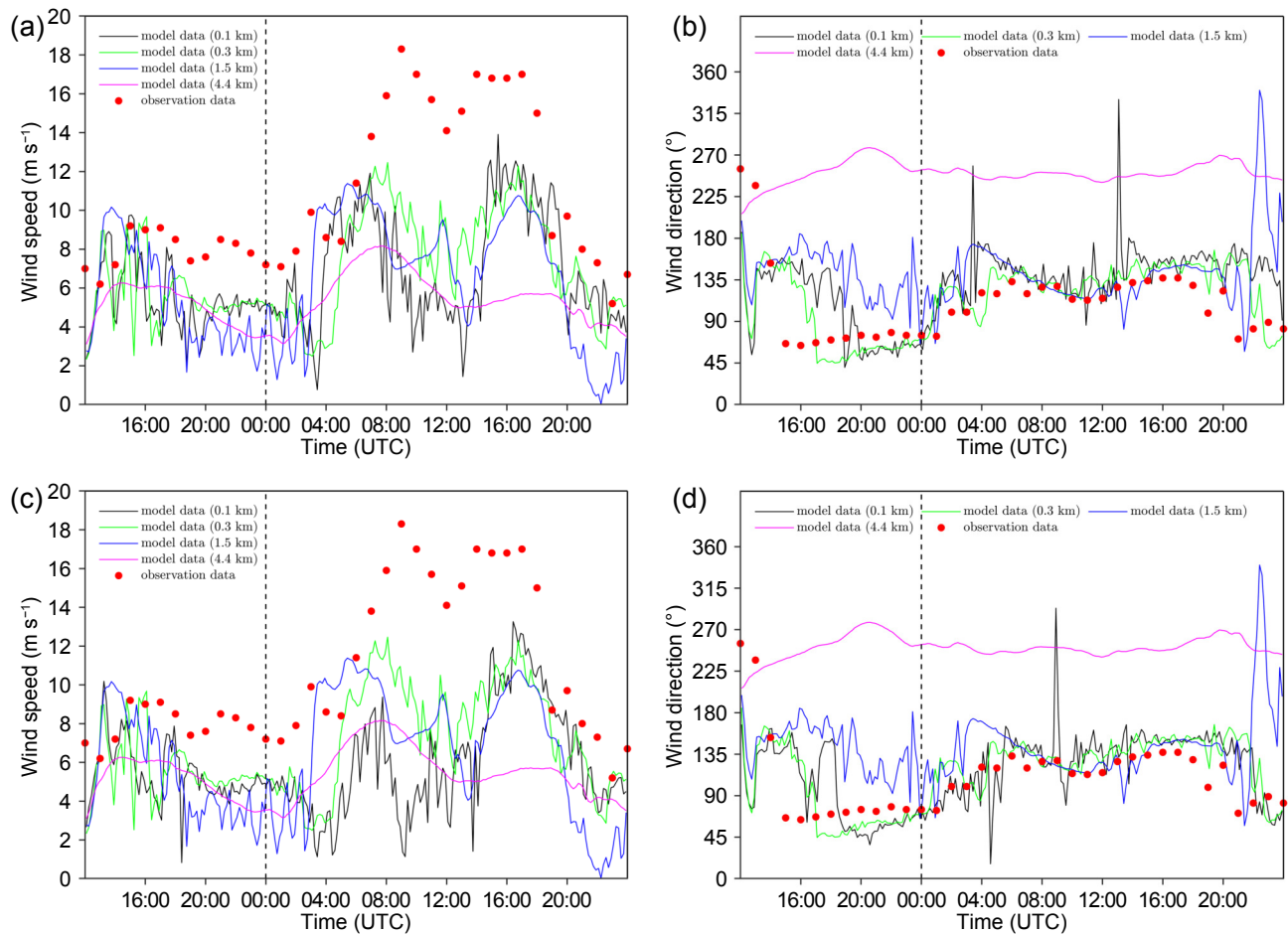
Fig. 13. As in Fig. 12 but for site 2.

scatter about small values due to the relative dominance of fluctuations. Unfortunately, the value of the parameter when derived from the model in the innermost domain similarly correlates fairly plainly with the mean absolute wind speed during the windstorm event, giving better agreement for UNIFORM that in fact seems to simply reflect poor performance simulating the wind strength. There is a contrast, however, between this and the period just before the wind rises at around 0400 UTC, and the period from around 1200–1800 UTC, when the wind is in a generally less disturbed, simple up-valley flow state. In this period, the ratio's value is higher for a given wind speed.

That $\overline{|\Delta s_{mau}|}$ and the mean-vector/mean-absolute ratio prove less informative than they did when calculating statistics over the entire grid suggests that the availability of significantly denser observational coverage would be desirable, either through greater deployment of point measurements, or via remote sensing solutions.

5. Summary and discussion

Simulations were carried out of a gale case in the lee of Cangshan Mountain, Yunnan, China, using MetUM, nesting to 100 m horizontal grid spacing. These revealed a trapped lee wave in the lee of Cangshan mountain and a downslope windstorm at the surface which separates to form a rotor flow, where the core of the rotor in fact takes the form of an along-valley flow over Erhai Lake (which fills the majority of the valley floor area), though with a backward wind component similar to the common 2D rotor concept.

A targeted smoothing method, which minimises the terrain information lost in the model as a result of the orographic smoothing necessary for the model to run stably, has been applied and tested using this case. Using a slope threshold defined from terrain that has been uniformly smoothed sufficiently for stable model running, and an iterative approach, this targets the strongest smoothing only over the steepest slopes, leaving areas where the slope is not critical minimally smoothed.

Simulations where targeted smoothing was applied in the innermost 100 m domain exhibited a wealth of extra granular detail in the flow, and quantitatively greater temporal and spatial variability. Significantly stronger extremes of wind, particularly on ridge crests, also occur. Coherent small scale accelerated flow features emerge in these simulations, that are absent when a uniform smoothing method is applied, since they originate from narrow channels running down the lee side of the mountain, that uniform smoothing would largely remove. These act to disturb a broad along-val-
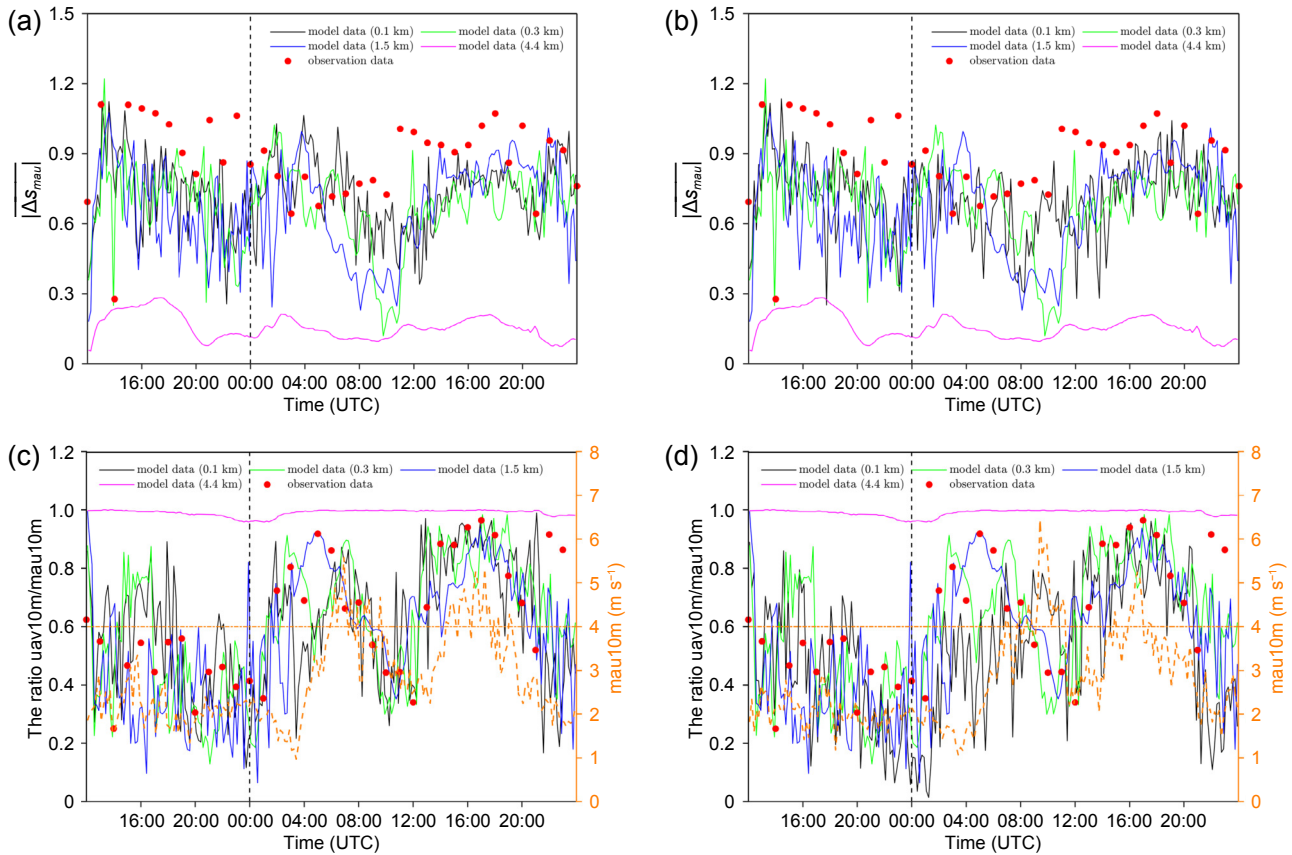
Fig. 14. (a, b) Average absolute speed-up values, $\overline{|\Delta s_{maul}|}$, across six observation sites that measured wind around Cangshan during the 23 January 2015 windstorm case, plotted as a function of time (red points). (c, d) Ratio of $\overline{|\mathbf{u}_{10m}|}$ to mean absolute wind speed over time across the same 6 sites (red points). In both panels, coloured lines are traces using data from the four domains of (a, c) the UNIFORM simulation, and (b, d) the TARG-INNERMOST simulation, calculated using the 6 grid points nearest to the 6 sites (domain is given by the colour key). An overlay of the mean absolute wind speed is added (orange, dashed) in (c) and (d) to make periods of low or high wind clear, with a threshold of 4 m s^{-1} included as a guide to the eye. A vertical dashed line indicates 0000 UTC.

ley flow occurring during the peak of the event. Highly coherent when uniform smoothing is used, this flow becomes significantly less strong and coherent with targeted smoothing.

The strength of these small scale flows seems to be responsible for an extension further east of the downslope windstorm, so that the observed windstorm's extension over Dali, a city on the western shore of Erhai Lake, is captured to a degree, including the peak wind. This is absent in the simulation with smoothing uniformly applied.

Quantitative analysis of variability filtered for different scales in the range up to 30 km indicates there is an increase in spatial variability at small to intermediate scales, consistent with the qualitatively new features introduced when targeted smoothing is used (such as the above channel outflows). This occurs at the expense of variability at large scales, and the disturbance of the larger scale along-valley flow is consistent with this migration of detail from the larger scales to intermediate scales.

Observations from a network of sites sampling variation at the mesoscale in the area, run by the Dali National Climate Observatory, were used to examine the performance of the simulations in reproducing the accelerated lee side flow,

and to characterise the spatial variability in the observations for comparison with the simulations. During the peak of the event, the winds in the downslope windstorm are only captured in the case where targeted smoothing was used in the innermost domain. In the innermost domain, the simulations encouragingly identify a slightly stronger signal in one measure used to quantify spatial variability during the peak period of the event. But only 6 observation sites were available for comparison with the simulation, yielding poor sampling that prevents such metrics from being very useful; better observational coverage is desirable.

Future work may include examination of the life cycle (initiation, termination) of the event. This may include analysis of high temporal resolution time series of the simulated winds. The impact of the simulation of Erhai Lake, which dominates the valley, and was found to be an important aspect in the treatment of the flow by Xue et al. (2020), is also desirable to understand. The long record of similar events at the same location enables a more general examination of mountain waves, downslope windstorms and rotors in the area. Placing the event in context with similar flows in other geographic/climatological locales would also be valu-

able, such as the Alps (Europe), Sierra Nevada or Colorado mountains (USA). High resolution, nested simulations such as this also afford the opportunity to examine the performance of parametrisations, which have to function across a range of resolutions.

The multiple resolutions that come with the nested approach further offer the chance to examine the relative value of different degrees of resolution enhancement; for instance, when targeted smoothing is used in the 300 m horizontal grid spacing domain, the model recovers a portion of the advantage offered by 100 m grid spacing, performing roughly equivalently against some observed variables or statistics (not shown). The effect of increasing vertical resolution has also not been examined. The impact of events such as the case examined here across spatial and time scales in terms of local, regional weather and climate effects is also desirable to understand and depends on parametrisation accuracy. Datasets like that produced here, in tandem with the enhanced coverage of instrumentation associated with the Dali National Climate Observatory enable detailed study of scalar and momentum flux via different processes, to support such investigations.

Following the development of the targeted smoothing approach, it has been exploited in a number of use cases at the Met Office and among international MetUM partners, ranging from sub-km scale nested simulations akin to those in this paper, to global MetUM ensembles, wherein significant enhancements to model stability have been realised without paying the significant cost in the fidelity of the terrain data that would otherwise be incurred.

REFERENCES

Belušić, D., M. Žagar, and B. Grisogono, 2007: Numerical simulation of pulsations in the bora wind. *Quart. J. Roy. Meteor. Soc.*, **133**, 1371–1388, https://doi.org/10.1002/qj.129.

Best, M. J., and Coauthors, 2011: The Joint UK Land Environment Simulator (JULES), model description - Part 1: Energy and water fluxes. *Geoscientific Model Development*, **4**, 677–699, https://doi.org/10.5194/gmd-4-677-2011.

Beusch, L., S. Raveh-Rubin, M. Sprenger, and L. Papritz, 2018: Dynamics of a Puelche foehn event in the Andes. *Meteor. Z.*, **27**, 67–80, https://doi.org/10.1127/metz/2017/0841.

Bougeault, P., and Coauthors, 2001: The MAP special observing period. *Bull. Amer. Meteor. Soc.*, **82**, 433–462, https://doi.org/10.1175/1520-0477(2001)082<0433:TMSOP>2.3.CO;2.

Boutle, I. A., J. E. J. Eyre, and A. P. Lock, 2014: Seamless stratocumulus simulation across the turbulent gray zone. *Mon. Wea. Rev.*, **142**, 1655–1668, https://doi.org/10.1175/MWR-D-13-00229.1.

Doyle, J. D., and D. R. Durran, 2002: The dynamics of mountain-wave-induced rotors. *J. Atmos. Sci.*, **59**, 186–201, https://doi.org/10.1175/1520-0469(2002)059<0186:TDOMWI>2.0.CO;2.

Doyle, J. D., and R. B. Smith, 2003: Mountain waves over the Hohe Tauern: Influence of upstream diabatic effects. *Quart. J. Roy. Meteor. Soc.*, **129**, 799–823, https://doi.org/10.1256/qj.01.205.

Doyle, J. D., and D. R. Durran, 2007: Rotor and subrotor dynamics in the lee of three-dimensional terrain. *J. Atmos. Sci.*, **64**, 4202–4221, https://doi.org/10.1175/2007JAS2352.1.

Durran, D. R., 1986: Another look at downslope windstorms. part I: The development of analogs to supercritical flow in an infinitely deep, continuously stratified fluid. *J. Atmos. Sci.*, **43**, 2527–2543, https://doi.org/10.1175/1520-0469(1986)043<2527:ALADWP>2.0.CO;2.

Edwards, J. M., and A. Slingo, 1996: Studies with a flexible new radiation code. I: Choosing a configuration for a large-scale model. *Quart. J. Roy. Meteor. Soc.*, **122**, 689–719, https://doi.org/10.1002/qj.49712253107.

Elvidge, A. D., and I. A. Renfrew, 2016: The causes of foehn warming in the lee of mountains. *Bull. Amer. Meteor. Soc.*, **97**, 455–466, https://doi.org/10.1175/BAMS-D-14-00194.1.

Elvidge, A. D., I. A. Renfrew, J. C. King, A. Orr, T. A. Lachlan-Cope, M. Weeks, and S. L. Gray, 2015: Foehn jets over the Larsen C ice shelf, Antarctica. *Quart. J. Roy. Meteor. Soc.*, **141**, 698–713, https://doi.org/10.1002/qj.2382.

Farr, T. G., and Coauthors, 2007: The shuttle radar topography mission. *Rev. Geophys*, **45**, RG2004, https://doi.org/10.1029/2005RG000183.

Farrugia, P. S., and A. Micallef, 2006: Comparative analysis of estimators for wind direction standard deviation. *Meteorological Applications*, **13**, 29–41, https://doi.org/10.1017/S1350482705001982.

Gary, J. M., 1973: Estimate of truncation error in transformed coordinate, primitive equation atmospheric models. *J. Atmos. Sci.*, **30**, 223–233, https://doi.org/10.1175/1520-0469(1973)030<0223:EOTEIT>2.0.CO;2.

Gohm, A., G. Zängl, and G. J. Mayr, 2004: South Foehn in the Wipp Valley on 24 October 1999 (MAP IOP 10): Verification of high-resolution numerical simulations with observations. *Mon. Wea. Rev.*, **132**, 78–102, https://doi.org/10.1175/1520-0493(2004)132<0078:SFITWV>2.0.CO;2.

Grisogono, B., and D. Belušić, 2009: A review of recent advances in understanding the meso- and microscale properties of the severe Bora wind. *Tellus A*, **61**, 1–16, https://doi.org/10.1111/j.1600-0870.2008.00369.x.

Grubišić, V., and J. M. Lewis, 2004: Sierra Wave Project revisited: 50 years later. *Bull. Amer. Meteor. Soc.*, **85**, 1127–1142, https://doi.org/10.1175/BAMS-85-8-1127.

Haid, M., A. Gohm, L. Umek, H. C. Ward, and M. W. Rotach, 2022: Cold-air pool processes in the Inn Valley during Föhn: A comparison of four cases during the PIANO campaign. *Bound.-Layer Meteorol.*, **182**, 335–362, https://doi.org/10.1007/s10546-021-00663-9.

Hastings, D. A., and P. K. Dunbar, 1999: Global land one-kilometer base elevation (GLOBE) digital elevation model. documentation, volume 1.0. key to geophysical records documentation (KGRD) 34. National Oceanic and Atmospheric Administration, National Geophysical Data Center, 325 Broadway, Boulder, Colorado 80303.

Jemmett-Smith, B. C., 2014: Cold air pools over complex terrain. PhD dissertation, School of Earth and Environment, University of Leeds.

Jiang, Q. F., and J. D. Doyle, 2008: Diurnal variation of downslope winds in Owens Valley during the Sierra Rotor Experiment. *Mon. Wea. Rev.*, **136**, 3760–3780, https://doi.org/10.1175/2008MWR2469.1.

Klemp, J. B., 2011: A terrain-following coordinate with smoothed coordinate surfaces. *Mon. Wea. Rev.*, **139**, 2163–2169, https://doi.org/10.1175/MWR-D-10-05046.1.

Kuzmić, M., B. Grisogono, X. M. Li, and S. Lehner, 2015: Examining deep and shallow Adriatic bora events. *Quart. J. Roy. Meteor. Soc.*, **141**, 3434–3438, https://doi.org/10.1002/qj.2578.

Lilly, D. K., and E. J. Zipser, 1972: The front range windstorm of 11 January 1972 a meteorological narrative. *Weatherwise*, **25**, 56–63, https://doi.org/10.1080/00431672.1972.9931577.

Lock, A. P., A. R. Brown, M. R. Bush, G. M. Martin, and R. N. B. Smith, 2000: A new boundary layer mixing scheme. Part I: Scheme description and single-column model tests. *Mon. Wea. Rev.*, **128**, 3187–3199, https://doi.org/10.1175/1520-0493(2000)128<3187:ANBLMS>2.0.CO;2.

Mayr, G. J., and L. Armi, 2010: The influence of downstream diurnal heating on the descent of flow across the Sierras. *J. Appl. Meteorol. Climatol.*, **49**, 1906–1912, https://doi.org/10.1175/2010JAMC2516.1.

Moore, G. W. K., 2016: The March 1972 northwest Greenland windstorm: Evidence of downslope winds associated with a trapped lee wave. *Quart. J. Roy. Meteor. Soc.*, **142**, 1428–1438, https://doi.org/10.1002/qj.2744.

Neiman, P. J., R. M. Hardesty, M. A. Shapiro, and R. E. Cupp, 1988: Doppler lidar observations of a downslope windstorm. *Mon. Wea. Rev.*, **116**, 2265–2275, https://doi.org/10.1175/1520-0493(1988)116<2265:DLOOAD>2.0.CO;2.

Orr, A., and Coauthors, 2021: Comparison of kilometre and sub-kilometre scale simulations of a foehn wind event over the Larsen C Ice Shelf, Antarctic Peninsula using the Met Office Unified Model (MetUM). *Quart. J. Roy. Meteor. Soc.*, **147**, 3472–3492, https://doi.org/10.1002/qj.4138.

Park, J.-R., J.-H. Kim, Y. Shin, S.-H. Kim, H.-Y. Chun, W. Jang, C.-L. Tsai, and G. Lee, 2022: A numerical simulation of a strong windstorm event in the Taebaek mountain region in Korea during the ICE-POP 2018. *Atmospheric Research*, **272**, 106158, https://doi.org/10.1016/j.atmosres.2022.106158.

Peltier, W. R., and J. F. Scinocca, 1990: The origin of severe downslope windstorm pulsations. *J. Atmos. Sci.*, **47**, 2853–2870, https://doi.org/10.1175/1520-0469(1990)047<2853:TOOSDW>2.0.CO;2.

Reinecke, P. A., and D. R. Durran, 2009: Initial-condition sensitivities and the predictability of downslope winds. *J. Atmos. Sci.*, **66**, 3401–3418, https://doi.org/10.1175/2009JAS3023.1.

Shaw, J., 2018: Numerical representation of mountains in atmo-

spheric models. PhD dissertation, Department of Meteorology, University of Reading.

Shaw, J., and H. Weller, 2016: Comparison of terrain-following and cut-cell grids using a nonhydrostatic model. *Mon. Wea. Rev.*, **144**, 2085–2099, https://doi.org/10.1175/MWR-D-15-0226.1.

Sheridan, P., S. Vosper, and P. Brown, 2017: Mountain waves in high resolution forecast models: Automated diagnostics of wave severity and impact on surface winds. *Atmosphere*, **8**, 24, https://doi.org/10.3390/atmos8010024.

Sheridan, P. F., and S. Vosper, 2012: High-resolution simulations of lee waves and downslope winds over the Sierra Nevada during T-REX IOP 6. *J. Appl. Meteorol. Climatol.*, **51**, 1333–1352, https://doi.org/10.1175/JAMC-D-11-0207.1.

Skamarock, W. C., 2004: Evaluating mesoscale NWP models using kinetic energy spectra. *Mon. Wea. Rev.*, **132**, 3019–3032, https://doi.org/10.1175/MWR2830.1.

Smith, R. N. B., 1990: A scheme for predicting layer clouds and their water content in a general circulation model. *Quart. J. Roy. Meteor. Soc.*, **116**, 435–460, https://doi.org/10.1002/qj.49711649210.

Steppeler, J., R. Hess, U. Schättler, and L. Bonaventura, 2003: Review of numerical methods for nonhydrostatic weather prediction models. *Meteorol. Atmos. Phys.*, **82**, 287–301, https://doi.org/10.1007/s00703-001-0593-8.

Strauss, L., S. Serafin, S. Haimov, and V. Grubišić, 2015: Turbulence in breaking mountain waves and atmospheric rotors estimated from airborne *in situ* and Doppler radar measurements. *Quart. J. Roy. Meteor. Soc.*, **141**, 3207–3225, https://doi.org/10.1002/qj.2604.

Večenaj, Ž., D. Belušić, V. Grubišić, and B. Grisogono, 2012: Along-coast features of Bora-related turbulence. *Bound.-Layer Meteorol.*, **143**, 527–545, https://doi.org/10.1007/s10546-012-9697-6.

Walters, D., and Coauthors, 2017: The met office unified model global atmosphere 6.0/6.1 and JULES global land 6.0/6.1 configurations. *Geoscientific Model Development*, **10**, 1487–1520, https://doi.org/10.5194/gmd-10-1487-2017.

Webster, S., A. R. Brown, D. R. Cameron, and C. P. Jones, 2003: Improvements to the representation of orography in the met office unified model. *Quart. J. Roy. Meteor. Soc.*, **129**, 1989–2010, https://doi.org/10.1256/qj.02.133.

Weller, H., and A. Shahrokhi, 2014: Curl-free pressure gradients over orography in a solution of the fully compressible Euler equations with implicit treatment of acoustic and gravity waves. *Mon. Wea. Rev.*, **142**, 4439–4457, https://doi.org/10.1175/MWR-D-14-00054.1.

Wilson, D. R., and S. P. Ballard, 1999: A microphysically based precipitation scheme for the UK meteorological office unified model. *Quart. J. Roy. Meteor. Soc.*, **125**, 1607–1636, https://doi.org/10.1002/qj.49712555707.

Wood, N., and Coauthors, 2014: An inherently mass-conserving semi-implicit semi-Lagrangian discretization of the deep-atmosphere global non-hydrostatic equations. *Quart. J. Roy. Meteor. Soc.*, **140**, 1505–1520, https://doi.org/10.1002/qj.2235.

Xue, H. L., J. Li, T. T. Qian, and H. P. Gu, 2020: A 100-m-scale modeling study of a gale event on the lee side of a long narrow mountain. *J. Appl. Meteorol. Climatol.*, **59**, 23–45, https://doi.org/10.1175/JAMC-D-19-0066.1.

Zängl, G., 2012: Extending the numerical stability limit of terrain-following coordinate models over steep slopes. *Mon. Wea. Rev.*, **140**, 3722–3733, https://doi.org/10.1175/MWR-D-12-00049.1.